ELSEVIER

International Journal of Solids and Structures 41 (2004) 5793–5820

INTERNATIONAL JOURNAL OF SOLIDS and STRUCTURES

www.elsevier.com/locate/ijsolstr

Contact rolling and deformation in granular media

Matthew R. Kuhn [a,*], Katalin Bagi [b]

[a] *Department of Civil and Environment Engineering, School of Engineering, University of Portland, 5000 N. Willamette Boulevard, Portland, OR 97203, USA*

[b] *Research Group for Computational Structural Mechanics, Hungarian Academy of Sciences, Dept. of Structural Mechanics, Technical University of Budapest, Müegyetem rkp. 3, K.mf. 35, H-1521 Budapest, Hungary*

Received 26 November 2003; received in revised form 16 March 2004
Available online 17 July 2004

Abstract

The paper considers rotations at different scales in granular materials: the rotations of individual particles, the rolling and rigid-rotation of particle pairs, the rotational interactions of a particle within its cluster of neighbors, and the rotation of material regions. Numerical, Discrete Element Method (DEM) simulations on two- and three-dimensional (2D and 3D) assemblies show that particle rotations are diverse, that they increase with strain until the material begins to soften, and that they are expressed in spatial patterns, even at small strains. The interactions of a pair of particles are a combination of three modes: a contact deformation mode, a contact rolling mode, and a mode of rigid pair motions. Definitions are presented for each mode, including four different definitions of contact rolling. A rolling curl is also defined, which describes the cumulative rolling of neighboring particles around a central particle or sub-region. At a larger scale, material deformation and rotation are measured within small sub-regions of material, and the material deformation can be attributed to separate contributions of contact rolling, contact deformation, and the rigid-rotation of particle pairs. The diversity and extend of contact rolling were measured in 2D and 3D simulations. A dominant rolling pattern was observed, which resembles the interactions of rolling gears. This pattern can extend to distances of at least six particle diameters from a central particle.
© 2004 Elsevier Ltd. All rights reserved.

Keywords: Granular media; Deformation; Rolling; Contact; Microstructure

1. Introduction

Particle rotations are known to have a fundamental influence on the behavior of granular materials. In presenting their results of experiments on plastic rods, Oda et al. (1982) concluded that "particle rolling is indeed a dominant microscopic feature, especially in the presence of inter-particle friction." Subsequent experiments have sought to characterize the manner and extent of particle rotations and their effects upon the mechanical behavior of granular materials, and much of this work is reviewed. The current study

* Corresponding author. Fax: +1-503-943-7316.
E-mail addresses: kuhn@up.edu (M.R. Kuhn), kbagi@mail.bme.hu (K. Bagi).

0020-7683/$ - see front matter © 2004 Elsevier Ltd. All rights reserved.
doi:10.1016/j.ijsolstr.2004.05.066

characterizes particle rotations and rolling in granular materials by considering a hierarchy of rotational effects: the rotations of individual particles, the rotational interactions of particle pairs, the rotational interactions of a particle within its cluster of neighbors, and the rotations of larger material regions. Although our intent is not to develop a comprehensive account of particle rotations and their effects, we will attempt to clarify certain aspects of behavior and to fill in gaps in the current understanding. Our work is primarily experimental, and it is based upon rational definitions of such notions as granular deformation, rolling, material rotation, and material curl when applied to a discrete, granular media. Discrete Element Method (DEM) simulations are presented as a means of exploring and quantifying granular deformation and rolling in a realistic setting. The simulations are both two- and three-dimensional (2D and 3D), and they were conducted on circular, non-circular, spherical, and non-spherical particle assemblies.

The paper is organized in the following manner, with our original developments appearing primarily in Sections 3–5:

- In Section 2, we consider the rotations of particle units. We describe the experiments that are cited throughout the paper, and we corroborate the results of previous studies concerning statistical measures of particle rotations. We also illustrate a form of spatial patterning in the particle rotations.
- In Section 3, we consider the interactions of particle pairs. We summarize and apply previous work by the authors, in which we have distinguished and defined three forms of contact interactions: contact deformation, contact rolling (which we define in alternative ways), and rigid-rotation of the particle pair. All three motions are usually active at each contact at the same time, and we present experimental results that quantify the various interactions and their inter-relationships. We consider the manner in which particle rotations and rolling affect material behavior, and we illustrate a dominant pattern in the rolling among particles.
- In Section 4, we define a micro-measure of the rolling between a particle and its cluster of nearest neighbors. This measure, akin to the curl in a continuous media, is measured in experiments, and the results are compared with those in Section 3.
- In Section 5, we derive expressions for the deformation and rotation of discrete material sub-regions of 2D assemblies. The material rotations are compared with the particle rotations, and the material deformation is partitioned so that we can measure the separate effects of contact deformation, contact rolling, and the rigid-rotation of particle pairs.

2. Particle rotations

As a granular material is deformed, grains interact with each other through their contacts. These interactions are produced by the translations and rotations of the grains. In this section, we consider the rotations of the individual grains, statistical measures of these rotations, and the patterning of these particle rotations. In later sections, we discuss the rotational interactions of particle pairs, clusters, and regions. Particle rotations have been measured in 2D laboratory models, in numerical (DEM) simulations, and in 3D physical experiments (for example, Oda et al., 1982; Bardet, 1994; Calvetti et al., 1997; Daudon et al., 1997; Misra and Jiang, 1997; Lanier, 2001; Marcher and Vermeer, 2001; Matsushima et al., 2003). Experiments have consistently shown that, although particle rotations may be very large, the mean rotation of the particles within a large assembly is nearly equal to the mean, continuum spin of the assembly. The equivalence of mean-field rotation and the particle rotation has also been reported under conditions of non-uniform shearing. For example, Bardet (1994) conducted biaxial DEM simulations on a 2D assembly that had flexible side boundaries and rigid upper and lower platens. A persistent shear band spontaneously appeared under these conditions. Although particle rotations within the shear band were large and had a predominant direction, the mean particle rotation of the entire assembly was nearly zero. In their DEM

tests, Matsushima et al. (2003) found that the mean grain rotation and the continuum rotation were nearly equal, even within a shear band. Kuhn (1999) performed DEM shearing tests on a 2D assembly of circular disks and produced highly non-uniform patterns of shearing by applying body forces on the assembly. Even under conditions of large gradients in the shearing strain, the particle rotations were, on average, nearly equal to the mean-field rotation. Two studies have shown a difference, however, between the mean particle and mean-field rotations. In the special 2D simulations of Calvetti et al. (1997) the mean particle rotation was found to drift from the mean-field rotation. During those tests, the principal stress axes were continually rotated, which produced a progressively larger drift in the average particle rotation. Recently, Jenkins and La Ragione (2003) reported that in their triaxial compression simulations, the average spin of particles differed from the overall assembly rotation.

Although the conformance of the mean-field and mean-particle rotations may suggest a certain order among the rotations, this order is contradicted by the consistent observation of substantial variability among individual rotations. Experiments have shown that particle rotations are large and that the magnitude and variation of rotations increases with increasing strain (Oda et al., 1982; Bagi, 1993; Bardet, 1994; Misra and Jiang, 1997; Calvetti et al., 1997; Lin and Ng, 1997; Dedecker et al., 2000; Lanier, 2001; Kuhn, 2004). Even particle rotations in regular, hexagonal packings of coins and plastic rods have been found to be both large and diverse (Tamura et al., 1998; Khidas et al., 2001). Investigators have used the statistical standard deviation of the particle rotations as a measure of their magnitude and of the fluctuation of individual rotations from the mean. As an example, Dedecker et al. (2000) measured the particle spin rates in numerical biaxial tests on circular particles. At large compressive strains, the standard deviation of the particle spin was as large as twenty times the strain rate. In experiments on wood rods, Calvetti et al. (1997) also observed large fluctuations from the mean and found that the standard deviation of particle rotations increased in a consistent and nearly linear manner with increasing strain. Although evidence of rotation variability is now abundant at larger strains, the experimental record provides less evidence of the variability of particle rotations at small strains. This scarcity is likely due to the difficulty of measuring the initial particle velocities in physical experiments.

2.1. Computer simulations

To investigate the mechanical roles of rotation, rolling, and deformation, we conducted numerical, DEM simulations on five large two- and three-dimensional assemblies of densely compacted particles (see Cundall and Strack, 1979 for algorithm details). Although our primary focus will be on the more realistic 3D simulations, we conducted experiments on simpler 2D assemblies so that spatial patterning could be more easily observed, and so that we could directly measure the function of inter-particle rolling in the deformation of granular media.

Two 2D assemblies were tested: an assembly of disks and an assembly of ovals, each with 10,816 particles (Table 1). Three 3D assemblies were also tested, each containing 4096 spheres or non-spherical (oblate or prolate) solids of revolution called *ovoids*. The oval and ovoid shapes are smooth and convex, closely

Table 1
Initial states of five assemblies

	2D assemblies		3D assemblies		
	Circles	Ovals	Spheres	Oblate	Prolate
Number of particles	10816	10816	4096	4096	4096
Void ratio, e	0.173	0.112	0.509	0.376	0.372
Solid fraction	0.853	0.899	0.663	0.727	0.729
Avg. coordination no.	8.82	5.59	5.57	8.97	9.24

resembling ellipses and spheroids, and their construction and numerical treatment are described elsewhere (Potapov and Campbell, 1998; Kuhn, 2003b). These shapes had the following aspect ratios: ovals, 1.35; oblate ovoids, 0.65–0.85; and prolate ovoids, 1.2–1.6. In all assemblies, a range of particle sizes was used: $0.5\overline{D}$–$1.7\overline{D}$ for the 2D assemblies, and $0.5\overline{D}$–$1.35\overline{D}$ for the 3D assemblies, where $\overline{D}$ is the mean particle size.

The dense square and cubic assemblies were compacted from initially sparse arrangements of particles. The sparse assemblies were isotropically densified by converging their periodic boundaries. Densification was also promoted by "turning off" contact friction during this process (as in Thornton and Antony, 2000; Roux and Combe, 2003) and by periodically energizing the assembly by assigning random particle velocities. Table 1 shows the initial void ratio, solid fraction, and average coordination number of each assembly.

All assemblies were tested in either biaxial (2D) or triaxial (3D) compression within their periodic boundaries: the assembly height was slowly reduced while keeping a constant average normal stress along the sides. During the loading tests a simple force mechanism was employed between contacting particles. Linear, elastic normal and tangential contact springs were assigned equal stiffnesses ($k_n = k_t$), and slipping between particles would occur whenever the contact friction coefficient of 0.50 was attained. Although the contact characteristics between solid granules are likely closer to Hertzian than to linear, which may affect the rotational behavior (Jenkins and La Ragione, 2003), our present study explores the relative intensities of the rolling motions without any pretense of replicating the behavior of a particular material. Rolling and rotation were allowed to occur freely at the contacts.

Fig. 1 shows the evolution of the deviator stress $q = \sigma_{33} - \sigma_{11}$ (or $\sigma_{22} - \sigma_{11}$ in 2D) during loading, where q is expressed in a dimensionless form by dividing by the initial (negative) mean stress p_0. The strains ϵ_{22} and ϵ_{33} in the figure are Lagrangian, engineering strains, computed as the change in the assembly's height divided by its initial height. Elsewhere in the paper we employ an Eulerian strain increment, $\mathrm{d}\epsilon_{22}$ or $\mathrm{d}\epsilon_{33}$, as a small change in height relative to the current height. In order to analyze the incremental interactions of the particles, the positions of all particles were periodically stored at two nearby states, separated by a small strain increment $\mathrm{d}\epsilon_{33} = -5 \times 10^{-5}$. Pairs of these states were later used to compute the incremental rates of particle rotation, contact rolling, and other quantities.

The observed behavior in compression is typical for densely packed, unbonded granular materials (Fig. 1). The response is initially elastic, but plastic deformation soon dominates as the deviator stress approaches its peak state. The material is strongly dilatant at the peak state and during subsequent softening. At a vertical strain $-\epsilon_{33}$ of about 0.30, the material reaches a steady (critical) state of nearly constant stress

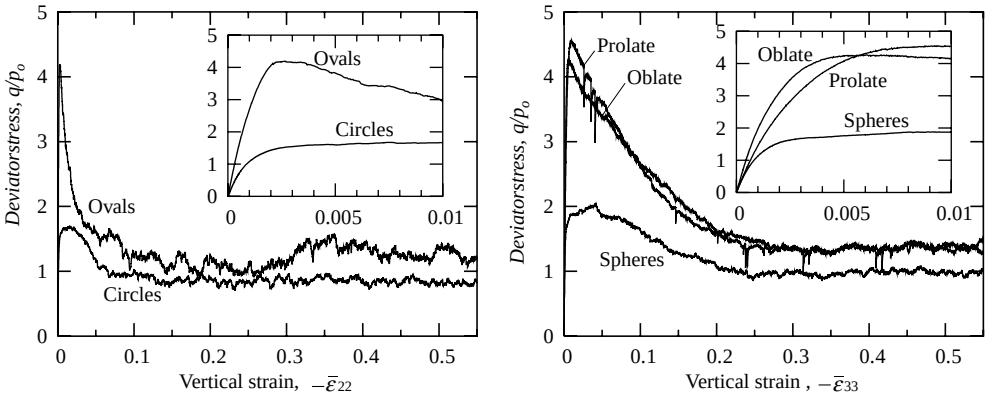

(a) Two-dimensional assemblies **(b)** Three-dimensional assemblies

Fig. 1. Loading behavior of all assemblies in biaxial or triaxial compression.

and volume. Localization is present in the 2D assemblies in the form of micro-bands at small strains and as shear bands at the peak state and beyond. Although we did not search for localization in the 3D assemblies, shear bands are unlikely, as the assembly was a fairly small cube, with a width less than 16 particle diameters.

2.2. Simulation results: particle rotations

For conditions of biaxial and triaxial compression, the mean (continuum) rotation is zero, and our experiments show that the mean rotation of the particles, although not zero, is very small. This result is evident in the second column ("Averaged rotation") of Table 2, which gives the averages of the mean particle rotations for the five assemblies at three strains. Each average is over the entire range of strains of a simulation and for the magnitude of the mean particle rotation at each strain:

$$\text{Averaged rotation} \equiv \underset{\epsilon_{33}=0 \text{ to } 0.50}{\text{Mean}} \left(\left| \underset{p=1 \text{ to } N}{\text{Mean}} (\mathrm{d}\boldsymbol{\theta}^p / |\mathrm{d}\epsilon_{33}|) \right| \right), \tag{1}$$

where p is the particle index, $\mathrm{d}\boldsymbol{\theta}^p$ is a particle rotation, and N is the number of participating particles in the assembly (either 4096 or 10,816, Table 1). Because the simulations did not include the influence of gravity, many particles are without contacts, and these non-participating, "floating" particles are excluded in our analysis of incremental effects. The particle rotations are expressed in a normalized form by dividing by the strain increment $\mathrm{d}\epsilon_{33}$ over which they are measured. Although the mean particle rotations are small, they are not zero. The small deviation is likely the result of averaging a population of individual rotations which exhibit an extreme variability. The mean rotation is certainly small when measured against the variability of the rotations: the mean rotation is typically less than one hundredth of the standard deviation of the rotations, as suggested by the standard deviations in the final two columns of Table 2 (the average in Eq. (1) is dominated by the range of strains between the peak and steady states).

The particle rotations exhibit large fluctuations from their mean. Fig. 2 shows the distribution of particle rotation rates $\mathrm{d}\theta_1$ within the oblate ovoid assembly at the peak stress. The standard deviation of the normalized rate $\mathrm{d}\theta_1/|\mathrm{d}\epsilon_{33}|$ is about 12, and over 5% of the particles are rotating 20 times faster than the vertical strain rate. Standard deviations of the rotation rates are summarized in the final three columns of Table 2 for the five assemblies at zero strain, at the peak stress, and during steady state deformation. Rotation rates at the peak state are from 20 to over 100 times greater than those at zero strain, but rotation rates are similar at the peak and steady states. These large increases in the particle rotation rates are consistent with the results of Calvetti et al. (1997), but we find that the rotation rates do not increase substantially after the peak strength has been reached. As would be expected, rotations are smaller at zero strain with non-spherical shapes than with spheres. At large strains, however, the rotation rates are similar for all three shapes.

Table 2
Mean and standard deviations of the particle rotation rates $\mathrm{d}\boldsymbol{\theta}^p$ for five assemblies

Assembly	Averaged rotation	$\mathrm{Std}(\mathrm{d}\theta_i^p)/\lvert\mathrm{d}\epsilon_{33}\rvert$[a]		
		Zero	Peak	Steady
Circles	0.10	0.96	19.5	32.0
Ovals	0.11	0.24	26.6	24.5
Spheres	0.10	0.65	12.4	16.3
Oblate ovoids	0.07	0.28	12.3	11.0
Prolate ovoids	0.10	0.26	9.1	13.2

[a] For two-dimensional assemblies, rotations $\mathrm{d}\theta_3^p$ are reported; for three-dimensional assemblies, rotations $\mathrm{d}\theta_1^p$ are reported.

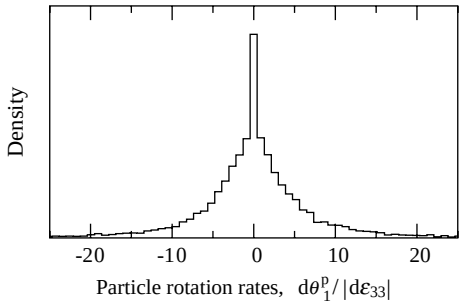

Fig. 2. Probability density of the particle rotation rates $d\theta_1^p/|d\epsilon_{33}|$ in the assembly of oblate ovoids at the peak stress condition.

2.3. Simulation results: spatial patterning of particle rotations

Fig. 3 shows the spatial distribution of the counter-clockwise rotations of particles in the assemblies of circles (Fig. 3a) and ovals (Fig. 3b). Only counter-clockwise rotations are shown in these monochrome plots, where the shading depends upon the dimensionless rotation rate $d\theta_3/|d\epsilon_{22}|$. Fig. 3a gives disk rotation rates at the start of biaxial compression ($\epsilon_{22} = 0$); Fig. 3b shows oval rotation rates at the hardening strain $\epsilon_{22} = -0.0012$, when the deviator stress had reached about 70% of its peak value. Both figures show a pervasive feature of granular rotation at small strains: the most rapidly rotating particles are usually aligned in chain-like patterns oblique to the principal stress directions. These *rotation chains* are somewhat more sinuous at the larger strain, but allowing for their frequent crooks and staggers, some rotation chains can be traced across the full height and width of the assembly and join other chains across the periodic boundaries. The particles within counter-clockwise rotation chains are usually not touching each other, as this would produce intense sliding between particles. The chains are closely associated with micro-bands—thin granular regions of more intense shearing strain and dilation (Kuhn, 1999). These chains are also observed in the rolling curl plots of Section 4.5. After the appearance of a shear band, the rotation chains are obscured by the more intense rotations within the shear band, although rotation chains can also trend through a shear band.

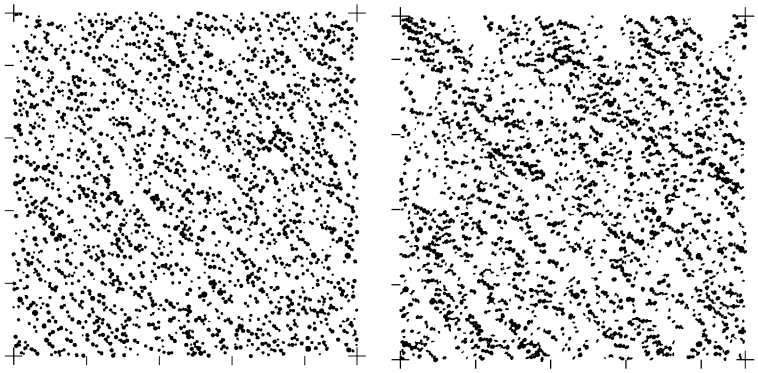

Fig. 3. Rotation rates of circles and ovals at two strains during biaxial compression. The figures only show particles that are rotating counter-clockwise. In (a), the shaded circles have rotation rates that exceed $d\theta_3/d\epsilon_{22} = 0.6$; in (b), the shaded ovals have rotation rates that exceed $d\theta_3/d\epsilon_{22} = 1.0$.

3. Interactions of particle pairs

The motions of a contacting pair of particles can be characterized as a combination of three modal forms: a deformation mode that produces sliding and indentation at the contact, a rolling interaction, and a rigid body rotation (rigid-rotation) and translation of the pair. In this section, we define each of these three modes and we present experimental results that characterize their nature and relative importance.

3.1. Definitions of contact deformation, rolling, and rigid motion

Consider two particles, p and q, to which we assign the material reference points $\boldsymbol{\chi}^p$ and $\boldsymbol{\chi}^q$ (Fig. 4). These reference points are located at positions $\mathbf{x}^p$ and $\mathbf{x}^q$ relative to the global axes. The two particles are in contact, and the vectors $\mathbf{r}^p$ and $\mathbf{r}^q$ connect points $\boldsymbol{\chi}^p$ and $\boldsymbol{\chi}^q$ to the contact. Branch vector $\mathbf{l}$ connects the two reference points: $\mathbf{l} = \mathbf{r}^p - \mathbf{r}^q = \mathbf{x}^q - \mathbf{x}^p$. The contact is assumed to be point-like, with a contact area that is negligible compared to particle size. The particles undergo incremental translational and rotational movements $\mathrm{d}\mathbf{u}^p$, $\mathrm{d}\mathbf{u}^p$, $\mathrm{d}\boldsymbol{\theta}^p$, and $\mathrm{d}\boldsymbol{\theta}^q$ during time increment $\mathrm{d}t$. These four movement vectors are described by twelve scalar components, which form a 12-dimensional vector space of possible movements. In classical kinematics, the particles might be truly rigid, and, hence, prevented from inter-penetration (a non-holonomic constraint), but the behavior of granular materials is influenced by the local particle deformations at their contacts. The contact deformations $\mathrm{d}\mathbf{u}^{\mathrm{def}}$ are produced by the relative displacements of two material points, one on either side of the contact,

$$\mathrm{d}\mathbf{u}^{\mathrm{def}} = (\mathrm{d}\mathbf{u}^q - \mathrm{d}\mathbf{u}^p) + (\mathrm{d}\boldsymbol{\theta}^q \times \mathbf{r}^q - \mathrm{d}\boldsymbol{\theta}^p \times \mathbf{r}^p). \tag{2}$$

We refer to this displacement as a *contact deformation*, and it can be separated into components that are normal and tangent to the contact surface, producing indentation and sliding. The contact deformation could also be termed a "contact displacement," but it is distinct from the deformation of a material region, which is produced by the contact deformations and also by the rearrangements of the particles (Section 5). The contact deformation (2) has long been used in the analysis and simulation of granular media (Cundall and Strack, 1979; Molenkamp, 1984; Koenders, 1987; Chang and Misra, 1989), but the sub-space of deformation motions accounts for only three of the twelve degrees of freedom of a particle pair. The deformation motion is objective, since its scalar components would be properly reported by two observers having independent motions (Kuhn and Bagi, 2004). Because the contact deformation is objective, it may be used in a constitutive description of the contact force–deformation relationship.

Although contact deformation can be unambiguously defined, contact rolling can be construed in alternative ways. Several notions of rolling have already been advanced (as in Oda et al., 1982; Molenkamp, 1984; Bardet, 1994; Iwashita and Oda, 1998; Lanier, 2001), but these definitions are not generally applicable

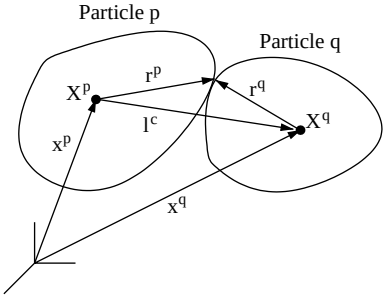

Fig. 4. Two contacting particles.

to 2D or 3D particles of arbitrary shape. We start with a general view of rolling, which admits numerous alternative forms: we view a contact rolling motion as any objective motion of a particle pair that is distinct from the contact deformation in Eq. (2). We have proposed three definitions of contact rolling, which are reviewed in the following paragraphs (Bagi and Kuhn, in press; Kuhn and Bagi, 2004). A fourth definition is also described.

The simplest definition of contact rolling is based on the relative rotation of a particle pair,

$$\mathrm{d}\boldsymbol{\theta}^{\mathrm{rel}} = \mathrm{d}\boldsymbol{\theta}^{q} - \mathrm{d}\boldsymbol{\theta}^{p}, \tag{3}$$

and, like the contact deformation motion in Eq. (2), the relative rotation (3) is clearly objective. The motion $\mathrm{d}\boldsymbol{\theta}^{\mathrm{rel}}$ can be separated into two components, one aligned with the contact normal $\mathbf{n}$ and the other perpendicular to $\mathbf{n}$:

$$\mathrm{d}\boldsymbol{\theta}^{\mathrm{rel,twist}} = (\mathrm{d}\boldsymbol{\theta}^{\mathrm{rel}} \cdot \mathbf{n})\mathbf{n}, \tag{4}$$

$$\mathrm{d}\boldsymbol{\theta}^{\mathrm{rel,roll,1}} = \mathrm{d}\boldsymbol{\theta}^{\mathrm{rel}} - (\mathrm{d}\boldsymbol{\theta}^{\mathrm{rel}} \cdot \mathbf{n})\mathbf{n}, \tag{5}$$

where the contact normal $\mathbf{n}$ is directed outward from particle p. The index "1" denotes the name *Type 1 rolling*, as described by the authors (Kuhn and Bagi, submitted for publication). The four motions (2)–(5) would be assigned opposite (negative) values if the indices p and q are exchanged. When plotting graphic visualizations of simulation results, we prefer alternative forms of Eqs. (4) and (5), since the values of these alternative forms do not depend upon the order of the indices:

$$\mathrm{d}\boldsymbol{\theta}^{\mathrm{rel,roll,1}} \times \mathbf{n}, \tag{6}$$

$$\mathrm{d}\theta^{\mathrm{rel,twist}} = \mathrm{d}\boldsymbol{\theta}^{\mathrm{rel}} \cdot \mathbf{n}, \tag{7}$$

where "twist" connotes a relative rotation about the contact normal $\mathbf{n}$.

A second form of rolling is based upon a particular averaging of the motions of two material points pc and qc, one attached to each of the particles at their contact (Fig. 5a). The two points are like two opposing teeth of inter-meshed gears, with the teeth moving in unison (in Fig. 5a, the two points lie on the dashed and solid particles at the times t and $t + \mathrm{d}t$, respectively). The average translation of the two points (e.g. the opposing gear teeth) is, of course, not objective, and its magnitude $\mathrm{d}u^{\mathrm{t\text{-}avr}}$, in a tangential direction $\mathbf{t}$,

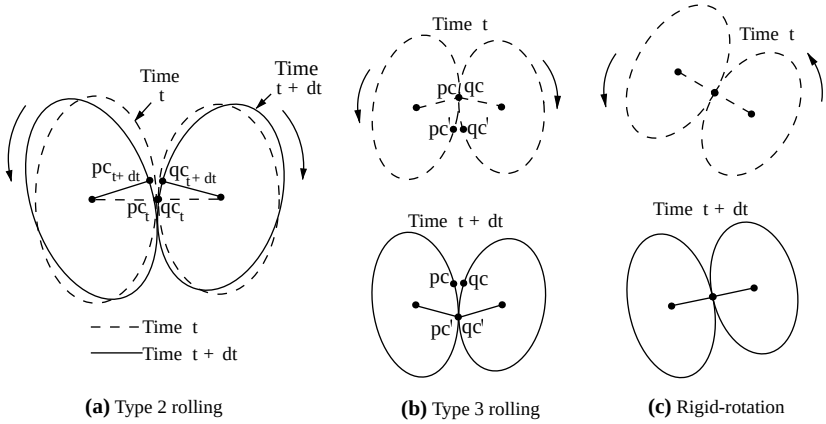

Fig. 5. Particle motions in rolling and in rigid-rotation.

$$\mathrm{d}u^{\mathbf{t}\text{-avr}} = \frac{1}{2}[(\mathrm{d}\mathbf{u}^p + \mathrm{d}\boldsymbol{\theta}^p \times \mathbf{r}^p)\cdot\mathbf{t} + (\mathrm{d}\mathbf{u}^q + \mathrm{d}\boldsymbol{\theta}^q \times \mathbf{r}^q)\cdot\mathbf{t}], \tag{8}$$

is also not objective. We can produce an objective average $\mathrm{d}u^{\mathbf{t}\text{-roll},2}$ by subtracting a common, rigid-body-like rotation of the pair (Bagi and Kuhn, in press):

$$\mathrm{d}u^{\mathbf{t}\text{-roll},2} = \frac{1}{2}\left[(\mathrm{d}\boldsymbol{\theta}^p\cdot\mathbf{z}^t)(\mathbf{r}^p\cdot\boldsymbol{\lambda}^t) + (\mathrm{d}\boldsymbol{\theta}^q\cdot\mathbf{z}^t)(\mathbf{r}^q\cdot\boldsymbol{\lambda}^t) - \frac{(\mathrm{d}\mathbf{u}^q - \mathrm{d}\mathbf{u}^p)\cdot\mathbf{t}}{\ell^{\perp t}}(\mathbf{r}^p + \mathbf{r}^q)\cdot\boldsymbol{\lambda}^t\right], \tag{9}$$

where the unit vectors $\mathbf{z}^t$ and $\boldsymbol{\lambda}^t$ depend upon the directions of the tangent vector $\mathbf{t}$ and the branch vector $\mathbf{l}$:

$$\boldsymbol{\lambda}^t = \mathbf{l}^{\perp t}/\ell^{\perp t}, \quad \mathbf{z}^t = \boldsymbol{\lambda}^t \times \mathbf{t}, \tag{10}$$

with

$$\mathbf{l}^{\perp t} = \mathbf{l} - (\mathbf{l}\cdot\mathbf{t})\mathbf{t}, \quad \ell^{\perp t} = |\mathbf{l}^{\perp t}|. \tag{11}$$

The quantity $\mathrm{d}u^{\mathbf{t}\text{-roll},2}$ is termed *Type 2 rolling*. Similar measures of rolling are associated with the normal direction $\mathbf{n}$ and a second tangent direction (say, direction $\mathbf{w}$), and these measures can be computed by substituting $\mathbf{n}$ or $\mathbf{w}$ in Eqs. (9)–(11). The scalar measures of $\mathbf{t}$, $\mathbf{w}$, and $\mathbf{n}$ rolling are independent of the ordering of the indices p and q. Unlike Type 1 rolling, which is a rotational quantity, Type 2 rolling is a translation, which we designate with the symbol $\mathrm{d}u$ instead of $\mathrm{d}\theta$ (cf., Eqs. (5) and (9)).

A third form of rolling is based upon the paths of two contact points as they travel across the two surfaces while the particles are moving. For example, when two inter-meshed gears rotate, the two contact points move from tooth to tooth around the two gears, even as each gear tooth is moving in the opposite direction. Fig. 5b shows the pairs of material points pc–qc and pc'–qc', which are the contact points on the two particles at the times t and $t' = t + \mathrm{d}t$. *Type 3 rolling* is defined as the average movement of the two contact points across the two surfaces. This form of rolling requires a knowledge of the local surface curvatures of the two particles at the contact (Montana, 1988; Kuhn and Bagi, 2004) and is given by

$$\mathrm{d}\mathbf{u}^{\mathrm{roll},3} = -(\mathbf{K}^p + \mathbf{K}^q)^{-1}\left[\mathrm{d}\boldsymbol{\theta}^{\mathrm{rel}} \times \mathbf{n} + \frac{1}{2}(\mathbf{K}^p - \mathbf{K}^q)\mathrm{d}\overline{\mathbf{u}}^{\mathrm{def}}\right], \tag{12}$$

where $\mathbf{K}^p$ and $\mathbf{K}^q$ are the surface curvature tensors, and $\mathrm{d}\overline{\mathbf{u}}^{\mathrm{def}}$ is the projection of $d\mathbf{u}^{\mathrm{def}}$ (defined by Eq. (2)) onto the tangent plane of the contact. Type 3 rolling is clearly objective, since it is a linear combination of the objective motions $\mathrm{d}\mathbf{u}^{\mathrm{def}}$ and $\mathrm{d}\boldsymbol{\theta}^{\mathrm{rel}}$. The vector $\mathrm{d}\mathbf{u}^{\mathrm{roll},3}$ lies in the tangent plane of the contact, and its value is independent of the ordering of indices p and q. Because it always lies in the tangent plane, vector $\mathrm{d}\mathbf{u}^{\mathrm{roll},3}$ is restricted to a two-dimensional sub-space of vectors. The rolling translation $\mathrm{d}\mathbf{u}^{\mathrm{roll},3}$ should, therefore, be supplemented with an auxiliary rolling quantity, say $\mathrm{d}\theta^{\mathrm{rel,twist}}$, to complete the full six-dimensional sub-space of objective motions (for example, the sub-space formed from the motions $\mathrm{d}\mathbf{u}^{\mathrm{def}}$, $\mathrm{d}\mathbf{u}^{\mathrm{roll},3}$, and $\mathrm{d}\theta^{\mathrm{rel,twist}}$). Motions that lie outside of this six-dimensional space, but within the 12-dimensional space of all motions, are non-objective (Kuhn and Bagi, submitted for publication).

A fourth form of rolling is more abstract than the others. As has been mentioned, the set of all objective motions is a six-dimensional vector sub-space that lies within the entire 12-dimensional space of motions for a particle pair. Rigid-body motions, described more fully in the next paragraph, also lie in the 12-dimensional space, but they are not objective. The fourth type of rolling is defined as the set of objective motions that are independent of (and orthogonal to) the vector sub-space of contact deformation motions in Eq. (2). By introducing this fourth form of rolling, we can project the motions of a particle pair onto three orthogonal sub-spaces: the contact deformation sub-space, the Type 4 rolling sub-space, and the rigid motion sub-space. This projection will be applied in Section 5 to explore the three corresponding sources of deformation in a granular media. *Type 4 rolling* is defined as the following rotation:

$$\mathrm{d}\boldsymbol{\theta}^{\mathrm{roll},4} = \frac{G}{G^2 - (\mathbf{s}\cdot\mathbf{l})^2}[(\mathbf{z}\otimes\mathbf{l})(\mathrm{d}\mathbf{u}^q - \mathrm{d}\mathbf{u}^p) - 2\mathbf{s}\times(\mathrm{d}\mathbf{u}^q - \mathrm{d}\mathbf{u}^p)] + \mathrm{d}\boldsymbol{\theta}^q - \mathrm{d}\boldsymbol{\theta}^p - \frac{1}{2}(|\mathbf{r}^q|^2 - |\mathbf{r}^p|^2)\Phi - \frac{1}{2}(\mathbf{l}\otimes\mathbf{s})\Phi, \tag{13}$$

where

$$\Phi = (1/H^p)\mathrm{d}\boldsymbol{\theta}^p + (1/H^q)\mathrm{d}\boldsymbol{\theta}^q, \tag{14}$$

$$H^p = \mathbf{r}^p\cdot\mathbf{l} + 2, \tag{15}$$

$$H^q = -\mathbf{r}^q\cdot\mathbf{l} + 2, \tag{16}$$

$$\mathbf{s} = \mathbf{r}^p + \mathbf{r}^q, \tag{17}$$

$$\mathbf{z} = \mathbf{r}^p\times\mathbf{r}^q, \tag{18}$$

$$G = |\mathbf{l}|^2 + 4. \tag{19}$$

This form of rolling resembles the relative rotation of Eq. (3), in that a permuting of the indices p and q reverses the direction of $\mathrm{d}\boldsymbol{\theta}^{\mathrm{roll},4}$. This characteristic can be corrected by using the following normal and tangential components:

$$\mathrm{d}\theta^{\mathrm{roll},4,n} = \mathrm{d}\boldsymbol{\theta}^{\mathrm{roll},4}\cdot\mathbf{n}, \tag{20}$$

$$\mathrm{d}\boldsymbol{\theta}^{\mathrm{roll},4,t} = \mathrm{d}\boldsymbol{\theta}^{\mathrm{roll},4}\times\mathbf{n}. \tag{21}$$

We have also derived a definition of the rigid motion of a particle pair (Kuhn and Bagi, submitted for publication). The definition gives a type of motion that is purely non-objective. That is, every motion of two particles (i.e., each element in the 12-dimensional vector space of possible motions) is the combination of an objective motion and a *purely* non-objective motion, which we refer to as the *rigid* component of motion. The set of all purely non-objective, rigid motions is a particular sub-space of the 12 degrees of freedom: the sub-space that is orthogonal to the sub-space of objective motions. The *rigid-rotation* is of interest in the current work (Fig. 5c), and it is defined as

$$\mathrm{d}\boldsymbol{\theta}^{\text{rigid-rot}} = \frac{1}{G}\left[\mathbf{l}\times(\mathrm{d}\mathbf{u}^q - \mathrm{d}\mathbf{u}^p) + 2(\mathrm{d}\boldsymbol{\theta}^p + \mathrm{d}\boldsymbol{\theta}^q) + \frac{1}{2}\mathbf{l}\cdot(\mathrm{d}\boldsymbol{\theta}^p + \mathrm{d}\boldsymbol{\theta}^q)\mathbf{l}\right], \tag{22}$$

where $G = |\mathbf{l}|^2 + 4$. The rigid-translation is defined elsewhere (Kuhn and Bagi, submitted for publication).

3.2. Simulation results: particle rotations and contact deformation

Past experimental programs have demonstrated that particle rotations reduce the stiffness and strength of 2D particle assemblies. We briefly review this evidence and then provide other experimental results that characterize the stiffening effect, with particular attention to 3D assemblies and to the 2D assembly of ovals.

The mechanical effects of particle rotations have been established in two types of numerical experiments. In one approach, the rotations are numerically restricted with the use of rotational springs or are prevented altogether (Bardet, 1994; Calvetti et al., 1997; Oda et al., 1997; Iwashita and Oda, 1998). The resulting strength and stiffness exceed those in control experiments with unrestrained rotations. In a second approach, measurements are taken of the incremental effects of the rotations upon the contact forces, which allows a partitioning of the stress increment into the separate effects of the particle rotations and

translations (Kuhn, 2004b). Such measurements suggest a substantial softening effect of the particle rotations.

A third type of evidence can be extracted from numerical experiments by analyzing the contact deformations $d\mathbf{u}^{\text{def}}$ that occur within the assembly (Eq. (2)). These contact deformations produce changes in the contact forces, which are the source of an assembly's incremental stiffness. Each contact deformation $d\mathbf{u}^{\text{def}}$ can be separated into parts that are due to the translations and the rotations of the pair of particles:

$$d\mathbf{u}^{\text{def}} = d\mathbf{u}^{\text{def,trans}} + d\mathbf{u}^{\text{def,rot}}, \tag{23}$$

$$d\mathbf{u}^{\text{def,trans}} = d\mathbf{u}^{q} - d\mathbf{u}^{p}, \quad d\mathbf{u}^{\text{def,rot}} = d\boldsymbol{\theta}^{q} \times \mathbf{r}^{q} - d\boldsymbol{\theta}^{p} \times \mathbf{r}^{p}. \tag{24}$$

We compare the quantities $d\mathbf{u}^{\text{def}}$, $d\mathbf{u}^{\text{def,trans}}$, and $d\mathbf{u}^{\text{def,rot}}$ among the thousands of inter-particle contacts in each of the five assemblies and at various strains. The comparisons are coefficients of correlation: a coefficient of zero indicates no correlation; coefficients of 1 and −1 indicate perfect and perfectly contrary correlations. The comparison can be broadened by separating $d\mathbf{u}^{\text{def}}$ into its normal and tangential components,

$$du^{\text{def},n} = d\mathbf{u}^{\text{def}} \cdot \mathbf{n}, \tag{25}$$

$$d\mathbf{u}^{\text{def},t} = d\mathbf{u}^{\text{def}} - du^{\text{def},n}\mathbf{n}. \tag{26}$$

and computing the corresponding contributions $du^{\text{def,trans},n}$, $du^{\text{def,rot},n}$, $d\mathbf{u}^{\text{def,trans},t}$, and $d\mathbf{u}^{\text{def,rot},t}$. An analysis of these comparisons leads to the following conclusions:

- Particle rotations have a softening effect by counteracting the influence of the particle translations. The translational contributions to contact deformation, $d\mathbf{u}^{\text{def,trans}}$, are negatively correlated with the rotational contributions $d\mathbf{u}^{\text{def,rot}}$. The coefficients of correlation range between −0.2 and −0.65 across all particle shapes and strains, and the correlations are most negative during material softening and at the steady state. Although one might expect the counter-action of translational and rotational contributions to be greater in the tangential direction than in the normal direction, this is not the case. For oval and ovoid shapes, the coefficients of correlation between $d\mathbf{u}^{\text{def,trans},n}$ and $d\mathbf{u}^{\text{def,rot},n}$ are even more negative, with values of −0.7 to −0.95 at large strains. That is, particle rotations reduce the changes in contact indentation that would otherwise be produced by particle translations.
- At zero strain, the contact deformations $d\mathbf{u}^{\text{def}}$ are closely correlated with the translational contributions $d\mathbf{u}^{\text{def,trans}}$, with coefficients of correlation greater than 0.82 for all shapes; but the contact deformations $d\mathbf{u}^{\text{def}}$ are entirely uncorrelated with the rotational contributions $d\mathbf{u}^{\text{def,rot}}$, with coefficients less than 0.01. Although the rotational fluctuations are uncorrelated with contact deformations, the fluctuations are substantial at zero strain (Section 2.2), and they reduce material stiffness (Kuhn, 2004b). The results indicate, however, that a micro-structural approach that intends to estimate material stiffness by assuming zero rotation should give a better estimate of the stiffness at small strains than at large strains. The correlation between $d\mathbf{u}^{\text{def}}$ and $d\mathbf{u}^{\text{def,trans}}$ is particularly strong for non-circular and non-spherical shapes at zero strain, with correlations greater than 0.95, which indicates that, at small strain, a zero-rotation assumption would be even better suited to such shapes.
- The opposite situation applies at large strains: the contact deformations $d\mathbf{u}^{\text{def}}$ correlate weakly with the translational contributions $d\mathbf{u}^{\text{def,trans}}$ but correlate strongly with $d\mathbf{u}^{\text{def,rot}}$. For example, at the steady (critical) state, the correlation between $d\mathbf{u}^{\text{def}}$ and $d\mathbf{u}^{\text{def,trans}}$ is only 0.2–0.4. The correlation between the contact deformations $d\mathbf{u}^{\text{def}}$ and the rotational contributions $d\mathbf{u}^{\text{def,rot}}$ is, however, much stronger, with coefficients between 0.55 and 0.7. That is, particle rotations assume a dominant role in contact deformation at large strains.

3.3. Simulation results: contact rolling and rigid-rotation

Four definitions of rolling were discussed in Section 3.1. The intensities of rolling Types 1, 2 and 3 were measured throughout the loading experiments on the five assemblies (Table 1), and the results are presented in this section. Type 4 rolling was used to characterize deformations within granular sub-regions, as discussed in Section 5.

Rolling Types 1, 2, and 3 give different measures of the rate of rotational interaction at the contacts. The Type 1 rolling in Eq. (6) is a relative rotational rate, whereas rolling Types 2 and 3 are translational rates. For pairs of circular and spherical particles of the same size, the three rates are multiples of each other (they differ in sign and by multiplicative factors of 2 and the shared radius). The three rolling rates are not equal for non-circular and non-spherical particles. However, in our tests on oval (2D) and ovoid (3D) shapes, we found a close correlation among the three types of rolling, with coefficients of correlation greater than 0.95. For this reason, we will only report the experimental results of Type 3 rolling, noting that large differences can occur among the three rolling measures for individual particle pairs.

Type 3 contact rolling is a vector quantity, a characteristic that must be considered when averaging these vectors over multiple contacts. We consider two tangential directions: a **t** direction and a **w** direction. Because the triaxial compressive loading in 3D tests is axisymmetric about the vertical $\mathbf{e}_3$ axis, we use a consistent tangent direction **w**,

$$\mathbf{w} = (\mathbf{e}_3 \times \mathbf{n})/|(\mathbf{e}_3 \times \mathbf{n}) \times \mathbf{n}|, \tag{27}$$

which is horizontal, and a consistent tangent direction **t** that lies in a vertical plane:

$$\mathbf{t} = \mathbf{w} \times \mathbf{n}. \tag{28}$$

In the rare case of a vertical contact ($\mathbf{e}_3 \cdot \mathbf{n} = 1$), the vector **w** in Eq. (27) does not exist, and all rolling takes place in the horizontal plane. In this case, **t** and **w** are assigned the $\mathbf{e}_1$ and $\mathbf{e}_2$ directions. We also report the rotational twists $\mathrm{d}\theta^{\mathrm{rel,twist}}$ about the contact normals **n** (Eq. (7)). The three scalar increments $\mathrm{d}\mathbf{u}^{\mathrm{roll},3} \cdot \mathbf{t}$, $\mathrm{d}\mathbf{u}^{\mathrm{roll},3} \cdot \mathbf{w}$, and $\mathrm{d}\theta^{\mathrm{rel,twist}}$ have a sign that is independent of the ordering of the particle indices (p and q, Fig. 4).

Tables 3 and 4 show the average intensities of **t**- and **w**-direction rolling among the thousands of contacts in each of the 3D assemblies at zero strain and at the state of peak stress (at $\epsilon_{33} = -0.02$). These rolling intensities are expressed as a standard deviation of the rolling rates in a dimensionless and normalized form by dividing by the mean particle diameter $\overline{D}$ and by the strain increment $|\mathrm{d}\epsilon_{33}|$. The tables also give the rates of twist $\mathrm{d}\theta^{\mathrm{rel,twist}}$ and the **t**- and **w**-direction rates of contact deformation (i.e., sliding, Eq. (2)). To compare twist with Type 3 rolling, we divide the twist by a factor of 4 to account for the factor of 1/2 in Eq. (12) and the ratio $|\mathbf{r}|/\overline{D}$, which is about 1/2 for most particles. We draw the following conclusions from the results in Tables 3 and 4:

Table 3
Contact rolling, twist, deformation, and rigid-rotation rates for 3D assemblies at zero strain

Description	Quantity, zero strain	Spheres	Ovoids	
			Oblate	Prolate
t-rolling	$\mathrm{Std}(\mathrm{d}\mathbf{u}^{\mathrm{roll},3} \cdot \mathbf{t})/|\mathrm{d}\epsilon_{33}|/\overline{D}$	0.15	0.060	0.066
w-rolling	$\mathrm{Std}(\mathrm{d}\mathbf{u}^{\mathrm{roll},3} \cdot \mathbf{w})/|\mathrm{d}\epsilon_{33}|/\overline{D}$	0.11	0.043	0.051
n-twist	$\mathrm{Std}(\mathrm{d}\theta^{\mathrm{rel,twist}})/|\mathrm{d}\epsilon_{33}|$	0.13	0.048	0.045
t-deformation	$\mathrm{Std}(\mathrm{d}\mathbf{u}^{\mathrm{def}} \cdot \mathbf{t})/|\mathrm{d}\epsilon_{33}|/\overline{D}$	0.16	0.18	0.18
w-deformation	$\mathrm{Std}(\mathrm{d}\mathbf{u}^{\mathrm{def}} \cdot \mathbf{w})/|\mathrm{d}\epsilon_{33}|/\overline{D}$	0.068	0.042	0.042
Rigid-rotation	$\mathrm{Std}(|\mathrm{d}\boldsymbol{\theta}^{\mathrm{rigid\text{-}rot}}|)/|\mathrm{d}\epsilon_{33}|$	0.26	0.12	0.11

Table 4
Contact rolling, twist, deformation, and rigid-rotation rates for 3D assemblies at the peak state

Description	Quantity, peak state	Spheres	Ovoids	
			Oblate	Prolate
t-rolling	$\mathrm{Std}(d\mathbf{u}^{\mathrm{roll},3} \cdot \mathbf{t})/\lvert d\epsilon_{33}\rvert/\overline{D}$	3.3	4.0	3.3
w-rolling	$\mathrm{Std}(d\mathbf{u}^{\mathrm{roll},3} \cdot \mathbf{w})/\lvert d\epsilon_{33}\rvert/\overline{D}$	3.8	4.2	3.3
n-twist	$\mathrm{Std}(d\theta^{\mathrm{rel,twist}})/\lvert d\epsilon_{33}\rvert$	3.9	3.9	2.7
t-deformation	$\mathrm{Std}(d\mathbf{u}^{\mathrm{def}} \cdot \mathbf{t})/\lvert d\epsilon_{33}\rvert/\overline{D}$	4.1	6.7	5.6
w-deformation	$\mathrm{Std}(d\mathbf{u}^{\mathrm{def}} \cdot \mathbf{w})/\lvert d\epsilon_{33}\rvert/\overline{D}$	3.6	4.8	4.0
Rigid-rotation	$\mathrm{Std}(\lvert d\boldsymbol{\theta}^{\mathrm{rigid\text{-}rot}}\rvert)/\lvert d\epsilon_{33}\rvert$	8.8	10.9	8.1

- At small strains, rolling is smaller among non-spherical particles than among spheres. At large strain, the rolling rates are about the same for all shapes.
- Rolling increases greatly with strain, just as the individual particle rotations become more rapid (Section 2.2). Rolling rates at the peak state are from 25 to 100 times greater than those at the start of loading.
- Rolling occurs with a similar intensity in the three directions **t**, **w**, and **n**. We view this as an unusual result: the assemblies were compressed in the vertical, $\mathbf{e}_3$ direction, but the rates of horizontal and vertical (tangent) rolling are about the same.
- Although the rates of contact rolling and contact deformation cannot be directly compared (rolling is an average movement, whereas deformation is a movement difference, Eqs. (2) and (12)), the results indicate that rolling becomes a relatively more significant mechanism at larger strains.
- As would be expected for axisymmetric vertical compression, tangential contact deformation (sliding) is greater in the vertical plane (**t**-direction) than in the horizontal, **w**-direction.

We also sought conditions that would promote or inhibit contact rolling, and we considered the influences of contact orientation, frictional slipping, contact force, and local material density. Our analyses showed that only material density has a significant effect on the rate of contact rolling:

- Fig. 6 shows the effect of contact orientation on the rates of contact rolling and contact deformation at the peak stress. For the vertical axisymmetric loading of these simulations, an orientation angle β can be conveniently measured from the horizontal $\mathbf{e}_1$–$\mathbf{e}_2$ plane (Fig. 6a), and symmetries are applied so that positive and negative β angles are folded onto the range 0–90°. The average magnitude of the rate of rolling, $|d\mathbf{u}^{\mathrm{roll},3} \cdot \mathbf{t}|$, is only modestly affected by the orientation β, with vertically oriented contacts having slightly greater rolling rates (Fig. 6b). This observation can be contrasted with the rates of tangential contact deformation (i.e., sliding), $d\mathbf{u}^{\mathrm{def}} \cdot \mathbf{t}$. Sliding is, on average, much more vigorous for horizontally oriented contacts ($\beta = 0$), whose average rate magnitude $|d\mathbf{u}^{\mathrm{def}} \cdot \mathbf{t}|$ is 2.5 times greater than the rate for vertically oriented contacts (Fig. 6c). Fig. 6d shows the averages of the signed values of sliding $d\mathbf{u}^{\mathrm{def}} \cdot \mathbf{t}$, where we have accounted for the anti-symmetric nature of sliding by plotting the averaged rate $\mathrm{sgn}(\beta)d\mathbf{u}^{\mathrm{def}} \cdot \mathbf{t}$. This rate is, of course, zero for horizontal contacts—there is no preferred sliding direction for a horizontal contact ($\beta = 0$). The maximum average sliding rate occurs at an angle β of 30–40° when the material has been loaded to the peak state.
- Contact rolling is as active among contacts that are undergoing frictional slipping as among those that are not.
- The rate of contact rolling is only slightly affected by the magnitude of the contact force. The coefficient of correlation between the rates $|d\mathbf{u}^{\mathrm{roll},3}|$ and the normal or tangential contact forces $|f^n|$ or $|\mathbf{f}^t|$ is less than 0.1 at all strains and for all particle shapes. This observation may be due to the contact law that was used in the simulations—linear, elastic normal and tangential springs—since the incremental contact rates are influenced by the same incremental contact stiffness, which is shared by all non-slipping contacts.

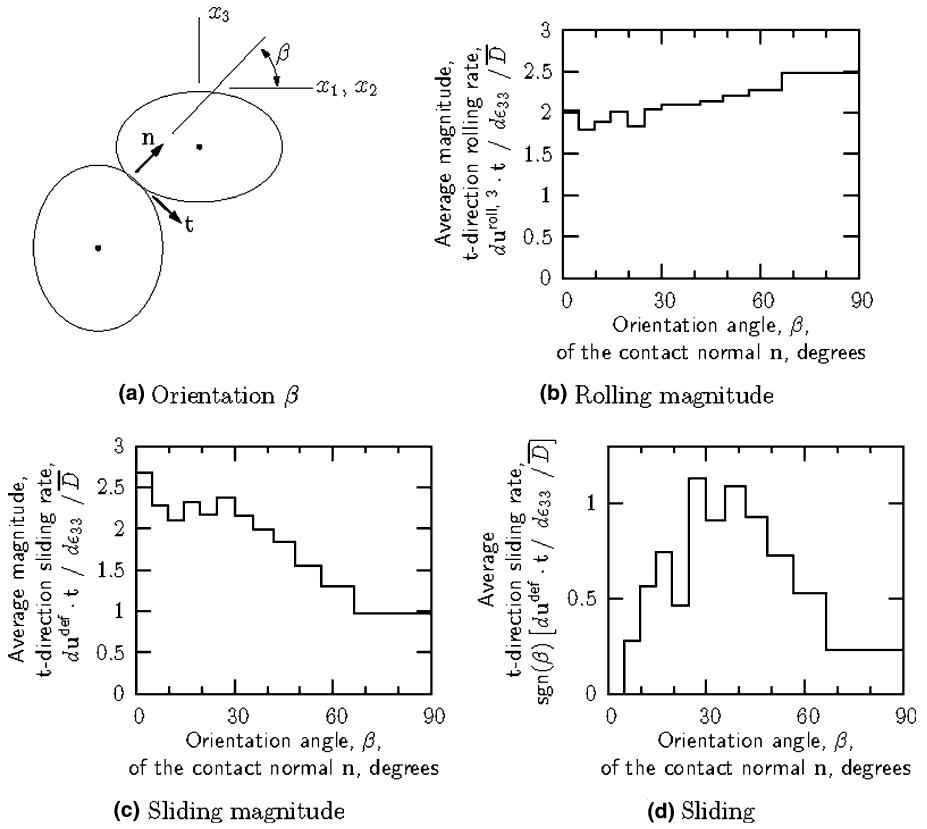

Fig. 6. Average contact rolling and sliding rates as a function of the contact orientation β at the peak stress: (a) orientation β; (b) rolling magnitude; (c) sliding magnitude; (d) sliding.

- The only factor that significantly affects the rate of contact rolling is the local contact density. In this regard, we counted the number of contacts around each pair of particles and measured its effect on the rolling rate $|d\mathbf{u}^{\text{roll},3}|$ of their common contact. The coefficient of correlation is between −0.05 and −0.35, indicating that the local contact density inhibits rolling.

The rigid-rotation of particle pairs is also an active mode of interaction (Eq. (22)). The intensity of this interaction mode is shown in Tables 3 and 4, which gives the dimensionless standard deviation of the rigid-rotation magnitudes, $|d\boldsymbol{\theta}^{\text{rigid-rot}}|$. The magnitudes of rigid-rotation are at least as large as those of contact rolling and deformation, although the larger values of $|d\boldsymbol{\theta}^{\text{rigid-rot}}|$ in the tables are due, in part, to our reporting of the full magnitude of the rigid-rotations, as compared with the component magnitudes of contact rolling and deformation. As with contact rolling and contact deformation, rigid-rotation is much larger at the peak state than at zero strain, at which rigid-rotation is slightly more active among non-spherical particles than among spheres. At larger strains, rigid-rotation has similar intensities for all shapes.

3.4. Simulation results: spatial patterning of contact rolling

A consistent spatial pattern was observed in the simulated deformation of 2D assemblies of circular disks and ovals. This pattern is illustrated in Fig. 7, which shows the rolling vectors among a subset of the 10,816

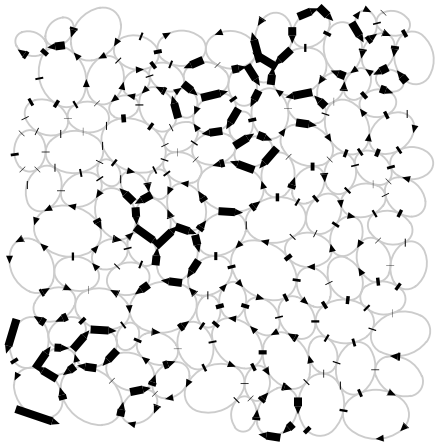

Fig. 7. Type 3 rolling rate vectors $d\mathbf{u}^{roll,3}$ for a small sub-region of ovals during biaxial compression. The figure is taken during material hardening, when the deviator stress had reached about 70% of the peak strength.

ovals during biaxial compression. The arrows represent the directions of the rolling vectors $d\mathbf{u}^{roll,3}$, and the arrow lengths are scaled to the magnitudes $|d\mathbf{u}^{roll,3}|$. Fig. 7 reveals that the rolling vectors around each particle are usually oriented in a common direction, either clockwise or counter-clockwise. For successive pairs of neighboring particles, the direction of rolling alternates from clockwise to counter-clockwise. We believe that this pattern is the dominant spatial pattern of movement in granular materials: it is observed at all strains and for all particle shapes. It is present before shear bands form, and it is present within the shear bands themselves. This pervasive spatial pattern operates at a length scale of as small as $1\overline{D}$—a single particle diameter. In Sections 4.4 and 4.5, we measure the distances to which this effect extends from an average particle.

In some respects, this rolling pattern can be likened to the motions among a set of rotating gears or cogs, since the rolling vectors around each gear would have a common direction, and this direction would alternate among neighboring gears. Although the motions of gears and particles bear some likeness, the analogy is not entirely appropriate, since no sliding can occur among inter-meshed gears, whereas rolling between particles occurs simultaneously with contact deformation (sliding and indentation), as well as with the rigid-rotations and translations of the particle pairs.

This gear-like pattern is more difficult to discern in three-dimensions, but it seems to be active in assemblies of spheres and ovoids, although perhaps to a more muted extent. As a simple measure of this pattern, we considered the subset of 3D particles with five contacts and found that with 22% to 33% of these particles, the rolling took place in the same direction for all five contacts (either clockwise or counter-clockwise), when rolling was measured about the $\mathbf{e}_1$ direction. If the direction of contact rolling was random, the likelihood of such unanimity would be 6.25%. The observation that, on average, 28% of particles satisfy this condition suggests that a gear-like rolling pattern is active in three-dimensional assemblies. This notion is also affirmed in Section 4.5.

Particle rolling also exhibits spatial patterning at a larger scale. Fig. 8 shows the spatial distributions of material deformation and contact rolling within the oval assembly at two compressive strains: at the hardening strain of $\epsilon_{22} = -0.0012$ and at the steady (critical) state of $\epsilon_{22} = -0.50$. The material deformations in Fig. 8a and b were computed as the deformations within small micro-regions of material—within the polygonal void cells, which form a complete covering of a 2D assembly—and the figures show the deformations in 18,000 and 7300 such micro-regions (Section 5, also see Bagi, 1996b and Kuhn, 1999). The

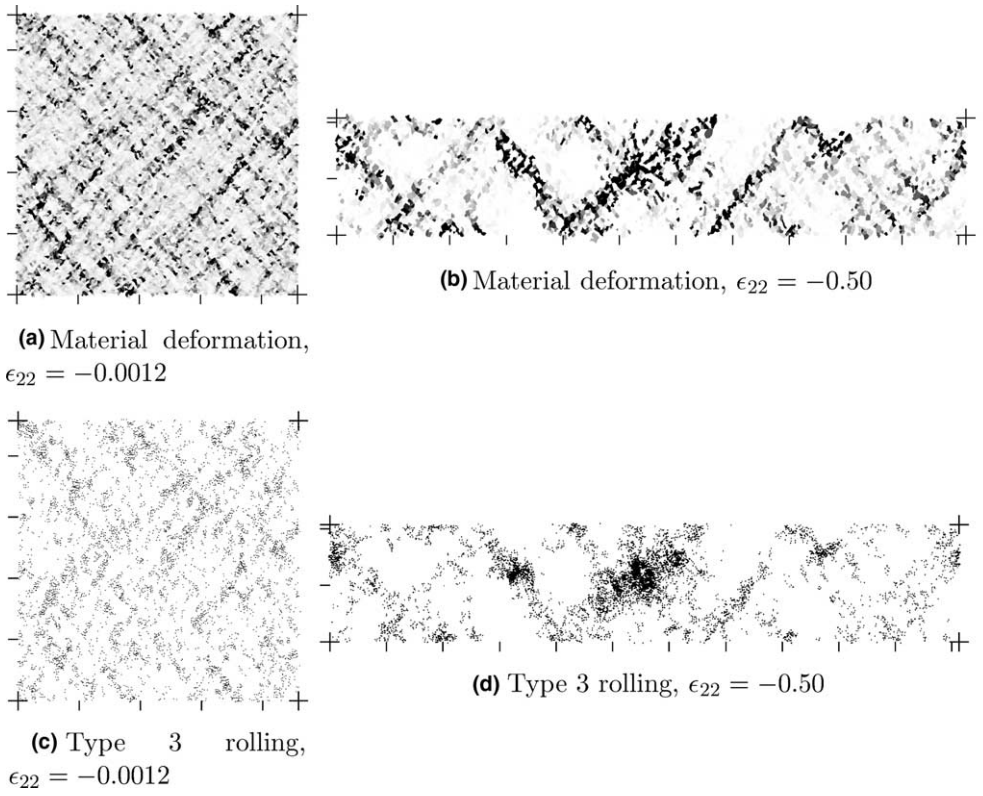

Fig. 8. Rates of material deformation and rolling at two strains. Figures (a) and (c) are during material hardening, when the deviator stress had reached about 70% of the peak stress. Figures (b) and (d) are at the steady (critical) state. The darkest regions in (a) are deforming more than 4 times faster than the mean rate (Eq. (29)); the darkest regions in (b) are deforming more than 10 times faster than the mean.

shading in Fig. 8a and b depends upon the contribution of each micro-region's rate of deformation tensor $\mathbf{D}^{\text{micro}}$ to the average assembly deformation $\mathbf{D}^{\text{average}}$:

$$\mathbf{D}^{\text{micro}} \cdot \mathbf{D}^{\text{average}} / |\mathbf{D}^{\text{average}}|^2, \tag{29}$$

where tensor $\mathbf{D}$ is the symmetric part of the (incremental) velocity gradient. Micro-bands are visible in the striated texture of Fig. 8a, when the material had been loaded to about 70% of its peak strength. Systems of thicker shear bands are seen in Fig. 8b, and these bands are inter-joined across the periodic boundaries.

The rolling vectors $d\mathbf{u}^{\text{roll},3}$ between oval particles are represented in Figs. 8c and 8d as miniature arrows, such as those in Fig. 7. Contact rolling is seen to coincide with the localized material deformation, and rolling is most intense among those particles that lie at the intersections of crossing shear bands (Fig. 7d).

4. A rolling curl

Because a gear-like pattern of particle motions appears to dominate in granular materials, we propose a measure of the combined extent of rolling translations at the contacts of a given, central particle. This measure can be interpreted as a discrete form of material curl, which may serve as a micro-level state

variable of material motion. In this section, we derive an expression for the average curl of a rolling vector field and introduce a simpler, approximate form of this average curl. Either form can be applied to the rolling of a granular sub-region (material cells) that is as small as an individual grain. Experimental measurements of this *rolling curl* are presented and discussed.

4.1. Discrete definition of rolling curl

The curl of a continuously differentiable vector field $\mathbf{v}$ at a point $\mathbf{x}$ can be defined as the limit of a surface integral:

$$\nabla \times \mathbf{v}(\mathbf{x}) = \lim_{V \to 0} \frac{1}{V} \int_{\partial \mathscr{B}} \mathbf{n} \times \mathbf{v} \, \mathrm{d}S, \tag{30}$$

where the region $\mathscr{B}$ vanishes around $\mathbf{x}$ and has a vanishing boundary surface $\partial\mathscr{B}$ and volume V (Fig. 9a). In this context, vector $\mathbf{n}$ is the outward unit normal of the surface $\partial\mathscr{B}$. The average curl $\overline{\nabla \times \mathbf{v}}$ within a finite region $\mathscr{B}$ is

$$\overline{\nabla \times \mathbf{v}} = \frac{1}{V} \int_{\partial \mathscr{B}} \mathbf{n} \times \mathbf{v} \, \mathrm{d}S. \tag{31}$$

Because the integral in Eq. (31) applies to the boundary of a finite region, we can relax the condition of differentiability and require that the field $\mathbf{v}$ is continuously differentiable on $\mathscr{B}$ except, perhaps, at zero-measure subsets, such as along surfaces within $\mathscr{B}$ and at lines (e.g., polyhedron edges) or at points (e.g., corners) on the exterior surface $\partial\mathscr{B}$. For a two-dimensional domain, the volume V would be replaced with the enclosed area A, and integration would be along the region's perimeter.

In order to interpret the curl of rolling in a finite granular region, we will identify a *material cell* $\mathscr{B}^p$ as a region (both solid and void) belonging to a single particle p, such that the union of all material cells forms a non-overlapping covering (i.e., a partition) of the entire assembly region (Fig. 9c). A material cell $\mathscr{B}^p$ would include all points that are closer to particle p than to any other particle (Bagi, 1996a,b). With this scheme, each material cell is a faceted region, with each face shared by two neighboring particles. A rolling vector $\mathrm{d}\mathbf{u}^{\mathrm{roll}}$ is associated with each contact of the particle p. The rolling vector could be based upon either of rolling Types 1, 2, 3, or 4, although we later apply a qualifying condition to the choice of rolling. Along the faces that correspond to these contacts, we assign values to a field $\mathrm{d}\mathbf{u}^{\mathrm{roll}}(\mathbf{x})$ along each face (for the purpose of this discrete calculation, an assignment of values $\mathrm{d}\mathbf{u}^{\mathrm{roll}}(\mathbf{x})$ is not required within the interior of $\mathscr{B}$, Eq. (31)). In this regard, we can assign a constant rolling vector field $\mathrm{d}\mathbf{u}^{\mathrm{roll}}(\mathbf{x})$ along each contact face: the single value of rolling $\mathrm{d}\mathbf{u}^{\mathrm{roll}}$ at the face's contact point (Fig. 9c). For a face that does not correspond to a pair of contacting particles, the rolling vector field would be zero.

Although we can use this piece-wise constant field $\mathrm{d}\mathbf{u}^{\mathrm{roll}}(\mathbf{x})$ on the boundary $\partial\mathscr{B}^p$, several alternative vector fields $\mathrm{d}\mathbf{u}^{\mathrm{roll}}(\mathbf{x})$ could also be assigned to points on the boundary. For example, with rolling Types 2 and 4, a rolling vector $\mathrm{d}\mathbf{u}^{\mathrm{roll}}$ could be calculated at each point $\mathbf{x}$ on a face (Type 3 rolling is, instead,

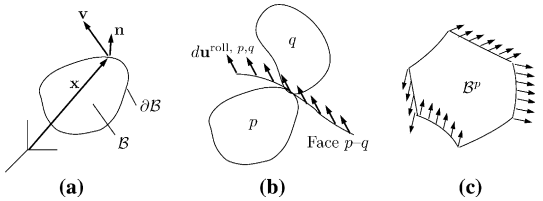

Fig. 9. Rolling curl within a material cell.

associated with the particles' surface curvatures at a particular contact point). A unique definition of the vector field on the interior of $\mathscr{B}$ is unnecessary: an interpretation of definition (31) requires only the existence and not the uniqueness of the field.

After assigning a vector field of rolling $\mathrm{d}\mathbf{u}^{\mathrm{roll}}(\mathbf{x})$ along the boundary of $\mathscr{B}^p$, we can define the corresponding *rolling curl* as

$$\mathrm{d}\boldsymbol{\rho}^p \equiv \overline{\nabla \times \mathrm{d}\mathbf{u}^{\mathrm{roll},p}} = \frac{1}{V^p}\int_{\partial\mathscr{B}^p} \mathbf{n} \times \mathrm{d}\mathbf{u}^{\mathrm{roll},p}\,\mathrm{d}S. \tag{32}$$

The assigned boundary vector field $\mathrm{d}\mathbf{u}^{\mathrm{roll},p}(\mathbf{x})$ may change abruptly along the edge lines and at the corners between the faces of material cell $\mathscr{B}^p$ and its neighboring cells—the underlying vector field may be discontinuous—but the existence of the integral (32) requires only that the field is continuously differentiable inside $\mathscr{B}^p$ and on the boundary surface $\partial\mathscr{B}^p$ except, perhaps, at such sets of zero measure.

The definition of rolling curl in Eq. (32) applies to a single material cell $\mathscr{B}^p$, but the average curl within a cluster of contiguous cells is simply the volume-weighted average

$$\mathrm{d}\boldsymbol{\rho}^{\mathrm{cluster}} = \frac{1}{\sum V^p}\sum V^p\,\mathrm{d}\boldsymbol{\rho}^p \tag{33}$$

of the rolling curls in the combined cells. This intrinsic character of the rolling curl is valid only if the rolling vector $\mathrm{d}\mathbf{u}^{\mathrm{roll}}$ along a face is independent of the ordering of the indices, say p and q, of the two particles on either side of the face. This condition is satisfied by rolling Types 2 and 3, by the Type 1 rolling in Eq. (6) and by the cross product of Type 4 rolling in Eq. (21).

4.2. Numerical estimation of the rolling curl

An exact calculation of Eq. (32) would require a numerical description of the material cells and their boundaries, which are difficult calculations, particularly for non-spherical particles. We have instead used a simpler numerical estimation of the rolling curl which avoids this difficulty, yet gives a meaningful measure of the average rate at which neighboring particles roll around a given, central particle. The tangent rolling motion $\mathrm{d}\mathbf{u}^{\mathrm{roll},p,q}$ between the central particle p and a contacting neighbor q (see Fig. 9b) can be thought to produce the rotation

$$\mathrm{d}\boldsymbol{\psi}^{\mathrm{roll},p,q} = \frac{\mathrm{d}\mathbf{u}^{p,q,\mathrm{roll}}\cdot\mathbf{y}^{p,q}}{\left(\mathbf{r}^{p,q}\times\mathbf{y}^{p,q}\right)\cdot\mathbf{w}^{p,q}}\mathbf{w}^{p,q}, \tag{34}$$

where $\mathbf{r}^{p,q}$ is the radial vector from particle p to its contact with q (the vector $\mathbf{r}^p$ in Fig. 4), $\mathbf{y}^{p,q}$ is the unit vector in the direction of $\mathrm{d}\mathbf{u}^{\mathrm{roll},p,q}$, and $\mathbf{w}^{p,q}$ is the unit vector for which the triad $(\mathbf{r}^{p,q},\mathbf{y}^{p,q},\mathbf{w}^{p,q})$ forms a right-hand orthogonal system:

$$\mathbf{y}^{p,q} = \frac{\mathrm{d}\mathbf{u}^{\mathrm{roll},p,q}}{\left|\mathrm{d}\mathbf{u}^{\mathrm{roll},p,q}\right|}, \quad \mathbf{w}^{p,q} = \frac{\mathbf{r}^{p,q}\times\mathbf{y}^{p,q}}{\left|\mathbf{r}^{p,q}\times\mathbf{y}^{p,q}\right|}. \tag{35}$$

The average of the imagined rotations (34) at the M^p contacts around p,

$$\overline{\mathrm{d}\boldsymbol{\psi}^p} = \frac{1}{M^p}\sum_{(p,q)}\mathrm{d}\boldsymbol{\psi}^{p,q,\mathrm{roll}}, \tag{36}$$

is the *estimated rolling curl* of the particle. The estimate can always be applied to convex particles, for which the tangent rolling vector $\mathrm{d}\mathbf{u}^{\mathrm{roll}}$ cannot be aligned with the radial vector ($\mathbf{r}^{p,q}\times\mathbf{y}^{p,q}\neq 0$), and Eq. (34) will always exist.

4.3. Simulation results: rolling curl

The objective rolling curl is strongly associated with the (non-objective) particle rotation: a rapidly rotating particle will likely be rolling vigorously at the contacts with its neighbors. Our results show that the coefficient of correlation between a particle's rolling curl $\overline{\mathrm{d}\boldsymbol{\psi}^p}$ and its rotation $\boldsymbol{\theta}^p$ is between 0.86 and 0.96 in the biaxial and triaxial loading of 2D and 3D assemblies.

We found that, on average, the rolling curl $\overline{\mathrm{d}\boldsymbol{\psi}^p}$ is roughly the same for all particle shapes, but that it is strongly inhibited by contact density. A three-dimensional particle with 4 contacts will have a rolling curl that is, on average, two to three times faster than that of a particle with 8 contacts.

4.4. Patterning of rolling curl

A gear-like spatial pattern of contact rolling was revealed in the plots of Section 3.4 (Fig. 7). This pattern can be quantified by considering the rolling curls $\mathrm{d}\boldsymbol{\psi}^p$ and $\mathrm{d}\boldsymbol{\psi}^s$ of pairs of particles (for example, particles p and s) that are separated by a distance. The intent is to correlate the rolling curl of particle pairs as a function of the separation between particles. For example, we would expect that the inner product $\mathrm{d}\boldsymbol{\psi}^p \cdot \mathrm{d}\boldsymbol{\psi}^s$ is, on average, negative for two adjoining particles, since a gear-like pattern would usually produce opposite curls for two contacting particles. We will determine if a correlation extends to greater distances. Rather than measure the geometric distance between two particles, we instead use a discrete, topologic distance (Kuhn, 2003a): the distance $d(p,s)$ between particles p and s is the minimum number of branch vectors (contacts) that must be traveled to reach one particle from the other. The integer distance $d(p,s)$ would equal 1 for two touching particles. Using this metric, a distance-dependent coefficient of correlation, $\Psi(\widehat{d})$, can be calculated in both 2D and 3D simulations:

$$\Psi(\widehat{d}) = \underset{\{(p,s):\, d(p,s)=\widehat{d}\}}{\operatorname{cov}} (\mathrm{d}\boldsymbol{\psi}^p, \mathrm{d}\boldsymbol{\psi}^s) \Bigg/ \underset{\{(p,s):\, d(p,s)=\widehat{d}\}}{\operatorname{cov}} (\mathrm{d}\boldsymbol{\psi}^p, \mathrm{d}\boldsymbol{\psi}^p). \tag{37}$$

The dimensionless correlation $\Psi(\widehat{d})$ is a quotient of covariances, with each covariance computed from the entire set of particle pairs (p,s) that are separated by a distance $\widehat{d}$. The covariance between a set of N vector pairs $(\mathbf{a},\mathbf{b})$ is defined as the average inner product,

$$\operatorname{cov}(\mathbf{a},\mathbf{b}) = \frac{1}{N}\sum (\mathbf{a}-\overline{\mathbf{a}})\cdot(\mathbf{b}-\overline{\mathbf{b}}), \tag{38}$$

where the mean values $\overline{\mathbf{a}}$ and $\overline{\mathbf{b}}$ are subtracted from each instance of $\mathbf{a}$ and $\mathbf{b}$. The correlation (37) at distance $\widehat{d}=0$ is simply 1, since a particle's curl is perfectly correlated with itself, for $d(p,p)=0$.

4.5. Simulation results: patterning of rolling curl

Results are presented in Tables 5 and 6 at zero strain and at the peak stress. The results show an alternating pattern of positive–negative–positive–etc. correlations, which correspond to a gear-like pattern of rolling. In the 2D assemblies, this pattern extends to distances $\widehat{d}$ of 6 or more for the average particle. That is, a particle's motion not only affects its immediate neighbors, but it also affects a much larger neighborhood, and the combined effects of all particles produce a coordinated, patterned system of alternating curls. The pattern extends to a greater average distance in 2D assemblies than in 3D assemblies, and the affected radius (i.e., the number of positive–negative alternations) is smaller at zero strain than at larger strains.

The spatial patterning of rolling curl is shown in Fig. 10 for assemblies of circles and ovals. The monochrome plot gives the magnitudes of rolling curl $|\overline{\mathrm{d}\boldsymbol{\psi}^p}|$ for those particles whose curl exceeds a

Table 5
Zero strain: correlation $\Psi(\widehat{d})$ of particle curls at increasing distances, $\widehat{d}$ (Eq. (37))

Distance $\widehat{d}$	2D assemblies		3D assemblies	
	Circles	Ovals	Spheres	Oblate
0	1.0	1.0	1.0	1.0
1	−0.55	−0.29	−0.37	−0.21
2	0.18	0.018	0.080	0.017
3	−0.036	0.0058	−0.0072	0
4	0.0059	0.0015	0.0008	0.0012
5	0.0029	0.0022	0	0
6	0	0.0014	0	0
7	0.0017	0.0010	0	0
8	0.008	0	0	0

Table 6
Peak stress: correlation $\Psi(\widehat{d})$ of particle curls at increasing distances, $\widehat{d}$ (Eq. (37))

Distance $\widehat{d}$	2D assemblies		3D assemblies	
	Circles	Ovals	Spheres	Oblate
0	1.0	1.0	1.0	1.0
1	−0.63	−0.51	−0.42	−0.33
2	0.33	0.20	0.14	0.091
3	−0.13	−0.060	−0.026	−0.013
4	0.047	0.020	0.0024	0.0029
5	−0.010	−0.0031	0.0011	0
6	0.0051	0.0035	0	0
7	0	0	0	0
8	0.0025	0.0010	0	0

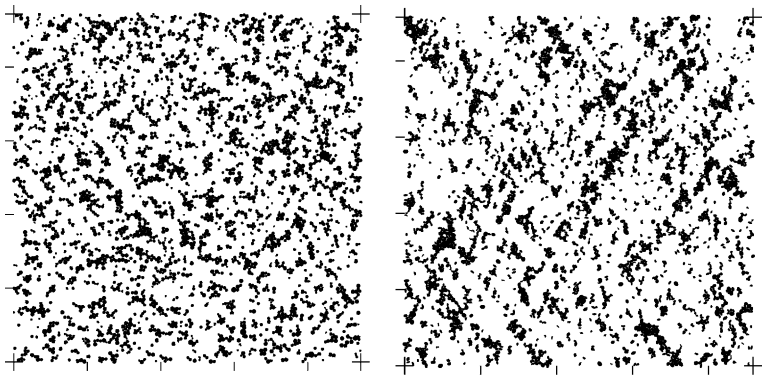

(a) Circles, $\epsilon_{22} = 0$ **(b)** Ovals, $\epsilon_{22} = -0.0012$

Fig. 10. Rolling curl rates of circles and ovals at two strains during biaxial compression. The figures depict the curl magnitude $|\mathrm{d}\overline{\psi^p}|/|\mathrm{d}\epsilon_{22}|$. In (a), the shaded circles have rates that exceed 0.3; in (b), the shaded ovals have rates that exceed 0.5.

threshold value. Fig. 10a is for circles at the start of biaxial compression ($\epsilon_{22} = 0$); Fig. 10b depicts ovals at the hardening strain $\epsilon_{22} = -0.0012$, when the deviator stress had reached about 70% of its peak value. Both figures show that rolling curl is not uniformly distributed within an assembly: particles with the most rapid

rolling curls are clustered in small groups of between 10 and 100 particles. Although these clusters are arranged randomly at small strains, without any obvious pattern, at larger strains, the clusters are elongated oblique to the directions of principal strain. Within the clusters, the curl occurs in the alternating positive–negative–positive pattern that was demonstrated in Tables 5 and 6.

5. Particle rotations and material deformation

In this section, we consider the material deformations and rotations within a granular material and their relation to the particle rotations. Just as contact deformation is distinct from the deformation of a granular region, particle rotations can differ from the rotations of an encompassing material region. As an example, the rotations of individual particles were seen to differ greatly from the zero material rotations of entire assemblies that were undergoing biaxial or triaxial compression (Section 2.2). The material deformations and rotations of a granular sub-region can be computed by tracking the translations of particles along the boundary of the sub-region (Bagi, 1996b). In two-dimensional assemblies, the average material deformation and rotation can be found within small, elemental polygon micro-regions called *void cells* (Fig. 11a), whose m corners lie at the centers of the adjoining particles (Bagi, 1996b; Kruyt and Rothenburg, 1996; Kuhn, 1999). The void cell partition of a 2D granular region (such as that in Fig. 11a) is the dual of the material cell partition that was discussed in Section 4.1 (Satake, 1993). The average incremental displacement gradient within a polygonal region, $\overline{\partial \mathbf{u}^{\text{cell}}/\partial \mathbf{x}}$, is computed as a linear combination of the set of relative translations $[\mathrm{d}\mathbf{u}^{\text{rel}}]$ of the m particle centers:

$$\overline{\mathrm{d}u_{i,j}^{\text{cell}}} = \frac{1}{A}\left[\mathrm{d}u_i^{\text{rel}}\right]^{\mathrm{T}}[Q]^m[b_j] + \frac{1}{A}[q_i]^{\mathrm{T}}[b_j]. \tag{39}$$

In this equation, A is the area of the m-polygon; $[\mathrm{d}u_i^{\text{rel}}]$ is an m-vector that contains the $\mathbf{e}_i$ components of the relative translations of adjacent corners (particle centers) taken as pairs around the polygon perimeter; $[b_j]$ is an m-vector that contains the $\mathbf{e}_j$ components of the m rotated sides of the polygon (i.e., the rotated branch vectors, $\mathbf{b} = \mathbf{Rl}$, $\mathbf{R} = \begin{bmatrix} 0 & 1 \\ -1 & 0 \end{bmatrix}$, as in Fig. 11b); and $[Q]^m$ is an $m \times m$ coefficient matrix (Kuhn, 1999). For the quadrilateral in Fig. 11b, the vectors in Eq. (39) are 4×1 and matrix $[Q]^4$ is 4×4. The first term on the right of Eq. (39) gives the incremental displacement gradient $\overline{\mathrm{d}u_{i,j}^{\text{cell}}}$ when each side (edge, branch vector) of the polygon deforms in an affine manner. In granular materials, the deformations along branch vectors are concentrated at the contacts—a departure from the affine condition. The second term on the right of Eq.

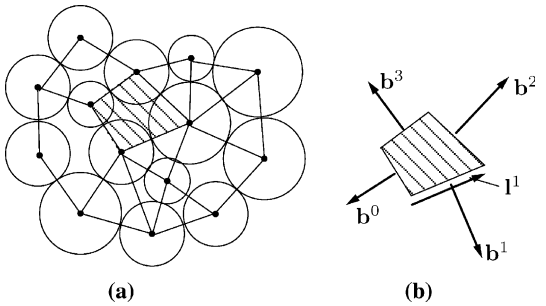

Fig. 11. (a) Polygonal void cells in a 2D granular media; (b) rotated branch vectors **b**.

(39) corrects for non-affine deformations along the polygon edges, with an m-vector $[q_i]$ that depends upon the translations and rotations of the boundary particles (Kuhn, 2004a).

5.1. Simulation results: material rotation

The histograms of Fig. 12 compare the particle rotations and void cell (material) rotations of the assembly of circular disks at two strains. Although the assembly rotation is zero under biaxial loading conditions, material rotation is non-uniform when viewed at a micro-scale, even at the start of loading. At zero strain, about 7% of the void cells are rotating at rates $\mathrm{d}u_{2,1} - \mathrm{d}u_{1,2}$ that exceed the rate of vertical compression, ϵ_{22}. These material rotations are largely organized in a micro-band patterning (Kuhn, 1999). At the peak stress, material rotations are quite large, with about 7% of the void cells rotating at rates greater than 10 times the rate of vertical compression. At small strain, the material (void cell) rotations are, on average, smaller and less varied than the particle rotations: the distributions of material rotation have greater peaks and smaller tails than those of the particle rotation rates. At the peak state, the distributions of material rotation and particle rotation are similar, with particle rotations being only modestly larger in their magnitude and scatter.

5.2. Partitions of material deformation

Several investigators have measured the deformations within such polygonal micro-regions (Kruyt and Rothenburg, 1996; Kuhn, 1999; Lanier and Jean, 2000; Roux and Combe, 2003). In the current study, we use Eq. (39) to investigate two partitions of the void cell deformations, to gain a better understanding of the source and nature of granular deformation. These partitions were applied in the simulations of biaxial compression of the 2D assembly of circular disks. This approach is a counterpart to the use of stress partitions to explore force transmission in granular materials (Cundall and Strack, 1983; Kuhn, 2004b). The deformation partitions are as follows:

(1) In the first partition, we separate the effects of relative disk translations that are aligned with and that are perpendicular to the contact normals. Each of the m relative movements $\mathrm{d}\mathbf{u}^{\mathrm{rel}}$ in Eq. (39) is the relative translation of two particle centers, say p and q, at adjacent corners of a polygon:

$$\mathrm{d}u_1^{\mathrm{rel},pq} = \mathrm{d}u_1^q - \mathrm{d}u_1^p \quad \text{and} \quad \mathrm{d}u_2^{\mathrm{rel},pq} = \mathrm{d}u_2^q - \mathrm{d}u_2^p. \tag{40}$$

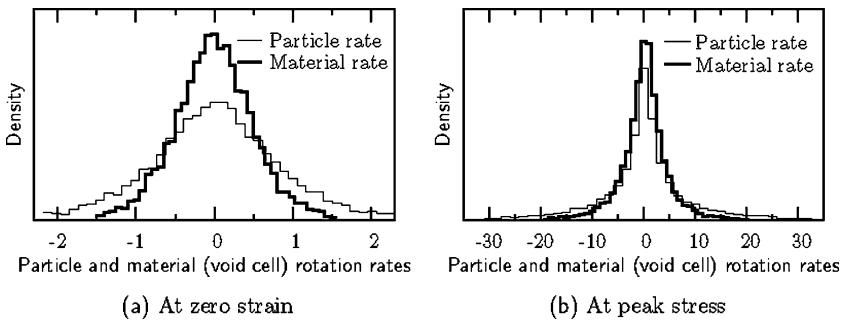

Fig. 12. Particle rotations and material (void cell) rotations in the 2D disk assembly. Probability densities are for the dimensionless particle rotations, $\mathrm{d}\theta_3^p/|\mathrm{d}\epsilon_{22}|$, and for the dimensionless void cell rotations, $(\overline{\mathrm{d}u_{2,1}^{\mathrm{cell}}} - \overline{\mathrm{d}u_{1,2}^{\mathrm{cell}}})/|\mathrm{d}\epsilon_{22}|$.

A relative translation $\mathrm{d}\mathbf{u}^{\mathrm{rel},pq}$ can be separated into components that are parallel and perpendicular to the contact normal $\mathbf{n}$:

$$\mathrm{d}\mathbf{u}^{\mathrm{rel},pq} = \mathrm{d}u^{\mathrm{rel},pq,n}\mathbf{n} + \mathrm{d}u^{\mathrm{rel},pq,t}\mathbf{t}. \tag{41}$$

The separate effects of these two parts are investigated by substituting them individually in Eq. (39) and measuring the corresponding deformations during biaxial compression:

$$\overline{\mathrm{d}u_{i,j}^{\mathrm{cell}}} = \overline{\mathrm{d}u_{i,j}^{\mathrm{cell,n}}} + \overline{\mathrm{d}u_{i,j}^{\mathrm{cell,t}}}, \tag{42}$$

which yields an additive partition of the void cell deformations.

(2) In the second partition, we separate the effects of the contact deformation, the Type 4 contact rolling, and the rigid-rotation of each pair of particles around the polygon's perimeter. These three types of motions were noted as forming orthogonal sub-spaces within the complete set of possible motions for a particle pair (Section 3.1). In two dimensions, the contact deformation, contact rolling, and rigid motion can be computed from the particle movements $\mathrm{d}\mathbf{u}^p$, $\mathrm{d}\mathbf{u}^q$, $\mathrm{d}\boldsymbol{\theta}^p$, and $\mathrm{d}\boldsymbol{\theta}^q$, as the matrix product

$$\begin{bmatrix} \mathrm{d}u_1^{\mathrm{def},pq} \\ \mathrm{d}u_2^{\mathrm{def},pq} \\ \mathrm{d}\theta^{\mathrm{roll},4,pq} \\ \mathrm{d}\theta_3^{\mathrm{rigid\text{-}rot},pq} \\ \mathrm{d}u_1^{\mathrm{rigid\text{-}trans},pq} \\ \mathrm{d}u_2^{\mathrm{rigid\text{-}trans},pq} \end{bmatrix} = [A]_{6\times 6} \begin{bmatrix} \mathrm{d}u_1^p \\ \mathrm{d}u_2^p \\ \mathrm{d}\theta_3^p \\ \mathrm{d}u_1^q \\ \mathrm{d}u_2^q \\ \mathrm{d}\theta_3^q \end{bmatrix}, \tag{43}$$

where the 6×6 matrix $[A]$ effects a linear combination of the six particle motions that are collected in the 6×1 vector on the right (Kuhn and Bagi, submitted for publication). The contents of the first four rows of $[A]$ are manifestations of Eqs. (2), (13), and (22).

The relative motions $\mathrm{d}\mathbf{u}^{\mathrm{rel}}$ in Eq. (39) are the differences in the translations of pairs of adjoining particles, say p and q, along the polygon sides, as in Eq. (40). By inverting matrix $[A]$ and multiplying by the left side of Eq. (43), we can express the relative translation (40) as a selective combination of contact deformation, contact rolling, and rigid-rotation effects:

$$\mathrm{d}u_1^{\mathrm{rel},pq} = \left(\left[A_{4,1..4}^{-1} \right] - \left[A_{1,1..4}^{-1} \right] \right) \begin{bmatrix} \mathrm{d}u_1^{\mathrm{def},pq} \\ \mathrm{d}u_2^{\mathrm{def},pq} \\ \mathrm{d}\theta^{\mathrm{roll},4,pq} \\ \mathrm{d}\theta_3^{\mathrm{rigid\text{-}rot},pq} \end{bmatrix}, \tag{44}$$

$$\mathrm{d}u_2^{\mathrm{rel},pq} = \left(\left[A_{5,1..4}^{-1} \right] - \left[A_{2,1..4}^{-1} \right] \right) \begin{bmatrix} \mathrm{d}u_1^{\mathrm{def},pq} \\ \mathrm{d}u_2^{\mathrm{def},pq} \\ \mathrm{d}\theta^{\mathrm{roll},4,pq} \\ \mathrm{d}\theta_3^{\mathrm{rigid\text{-}rot},pq} \end{bmatrix}, \tag{45}$$

where we have used the rows 1, 2, 4, and 5 and the columns 1, 2, 3, and 4 of the inverse matrix $[A]^{-1}$ to find the two components of relative translation, $\mathrm{d}u_1^{\mathrm{rel},pq}$ and $\mathrm{d}u_2^{\mathrm{rel},pq}$. For example, the single effect of contact rolling upon the relative translation $\mathrm{d}u_1^{\mathrm{rel},pq}$ is

$$\mathrm{d}u_1^{\mathrm{rel,roll},pq} = \left(A_{4,3}^{-1} - A_{1,3}^{-1} \right) \mathrm{d}\theta^{\mathrm{roll},4,pq}. \tag{46}$$

The cumulative rolling effect upon the void cell deformation, $\overline{\mathrm{d}u_{1,j}^{\mathrm{cell,roll}}}$, can then be found by assembling the corresponding effects (46) of each particle pair into an m-vector on the right of Eq. (39).

This approach yields the separate contributions of contact deformation, contact rolling, and rigid-rotation to the material deformation within a void cell:

$$\overline{\mathrm{d}u_{i,j}^{\mathrm{cell}}} = \overline{\mathrm{d}u_{i,j}^{\mathrm{cell,def}}} + \overline{\mathrm{d}u_{i,j}^{\mathrm{cell,roll}}} + \overline{\mathrm{d}u_{i,j}^{\mathrm{cell,rigid\text{-}rot}}}. \tag{47}$$

The rigid-translations in Eq. (39) make no contribution to $\overline{\mathrm{d}u_{i,j}^{\mathrm{cell}}}$, since their contribution to the relative motion $\mathrm{d}\mathbf{u}^{\mathrm{rel},pq}$ is zero for each particle pair (compare Eq. (43) with Eqs. (44) and (45), where the motions $\mathrm{d}u_1^{\mathrm{rigid-trans},pq}$ and $\mathrm{d}u_1^{\mathrm{rigid-trans},pq}$ are removed for this reason). The additive form in Eq. (47) is warranted by the nature of matrix $[A]$ in Eq. (43): the contact deformation, rolling, and rigid-rotation occur in orthogonal "directions" (the product of $[A]$ and its transpose $[A]^{\mathrm{T}}$ is block diagonal), so that the three motions contribute independently to the relative translations $\mathrm{d}\mathbf{u}^{\mathrm{rel},pq}$ in Eq. (40).

The contribution of contact deformations to the void cell (material) deformation, $\overline{\mathrm{d}u_{i,j}^{\mathrm{cell,def}}}$, can be further separated into the following three parts: a part $\overline{\mathrm{d}u_{i,j}^{\mathrm{cell,def},n}}$ due to the relative particle motions that are aligned with the contact normal; a part $\overline{\mathrm{d}u_{i,j}^{\mathrm{cell,def},t-\mathrm{elast}}}$ due to the tangential sliding motions that produce elastic deformations at the contacts (i.e., in the contact springs); and a part $\overline{\mathrm{d}u_{i,j}^{\mathrm{cell,def},t-\mathrm{slip}}}$ due to frictional slip at the contacts. The first part, $\overline{\mathrm{d}u_{i,j}^{\mathrm{cell,def},n}}$, is equal to the part $\overline{\mathrm{d}u_{i,j}^{\mathrm{cell},n}}$ of the first partition, Eq. (42).

5.3. Simulation results: material deformation

The two partitions of Eqs. (42) and (47) were investigated in the numerical simulation of 2D disks in biaxial compression, and the results are assembled in Tables 7 and 8. The tables give deformation rates at zero strain and at the peak stress. Both volumetric (dilatancy) and distortional rates are reported. Our analysis follows:

- Changes in the contact indentations tend to reduce an assembly's volume (Table 7, row A). Dilation, however, is largely the result of particle movements that are perpendicular to the contact normals (movements $\mathrm{d}u^{\mathrm{rel},pq,t}$ in Eq. (41); Table 7, row B). At both small and large strains, the normal movements produce compression, although the compressive influence is reduced at larger strains. The effect of the normal movements is counteracted by the increasingly dilatant influence of the tangential movements, which produces the net material dilation at large strains.

Table 7
Cumulative effect of the normal and tangential particle movements on the material deformation

		State	
		Zero	Peak
Dilation			
A	Normal movement, $\sum(\overline{\mathrm{d}u_{1,1}^{\mathrm{cell},n}} + \overline{\mathrm{d}u_{2,2}^{\mathrm{cell},n}})/\lvert\mathrm{d}\epsilon_{22}\rvert$	−0.81	−0.04
B	Tangential movement, $\sum(\overline{\mathrm{d}u_{1,1}^{\mathrm{cell},t}} + \overline{\mathrm{d}u_{2,2}^{\mathrm{cell},t}})/\lvert\mathrm{d}\epsilon_{22}\rvert$	−0.06	0.60
C	Total dilation, $(\mathrm{d}\epsilon_{11} + \mathrm{d}\epsilon_{22})/\lvert\mathrm{d}\epsilon_{22}\rvert \qquad \sum =$	−0.87	0.56
Distortion			
D	Normal movement, $\sum(\overline{\mathrm{d}u_{1,1}^{\mathrm{cell},n}} - \overline{\mathrm{d}u_{2,2}^{\mathrm{cell},n}})/\lvert\mathrm{d}\epsilon_{22}\rvert$	0.53	0.04
E	Tangential movement, $\sum(\overline{\mathrm{d}u_{1,1}^{\mathrm{cell},t}} - \overline{\mathrm{d}u_{2,2}^{\mathrm{cell},t}})/\lvert\mathrm{d}\epsilon_{22}\rvert$	0.60	2.52
F	Total distortion, $(\mathrm{d}\epsilon_{11} - \mathrm{d}\epsilon_{22})/\lvert\mathrm{d}\epsilon_{22}\rvert \qquad \sum =$	1.13	2.56

The results are for simulated biaxial compression of a 2D assembly of circular disks. The assembly deformation is a area-weighted tally of the micro-deformations within void cell regions.

Table 8
Cumulative effect of the contact deformation, rolling, and rigid movements on the material deformation

			State	
			Zero	Peak
Dilation				
Contact deformation, $\sum(\overline{du_{1,1}^{cell,def}} + \overline{du_{2,2}^{cell,def}})/\lvert d\epsilon_{22}\rvert$				
A	Normal movements		−0.81	−0.04
B	Tangential, elastic sliding		−0.03	0
C	Tangential, frictional slip		0	−0.14
D	Rolling, $\sum(\overline{du_{1,1}^{cell,roll}} + \overline{du_{2,2}^{cell,roll}})/\lvert d\epsilon_{22}\rvert$		0	−0.05
E	Rigid-rotation, $\sum(\overline{du_{1,1}^{cell,rigid\text{-}rot}} + \overline{du_{2,2}^{cell,rigid\text{-}rot}})/\lvert d\epsilon_{22}\rvert$		−0.35	0.79
F	Total dilation, $(d\epsilon_{11} + d\epsilon_{22})/\lvert d\epsilon_{22}\rvert$	$\sum =$	−0.87	0.56
Distortion				
Contact deformation, $\sum(\overline{du_{1,1}^{cell,def}} - \overline{du_{2,2}^{cell,def}})/\lvert d\epsilon_{22}\rvert$				
G	Normal movements		0.53	0.04
H	Tangential, elastic sliding		0.28	0
I	Tangential, frictional slip		0	0.72
J	Rolling, $\sum(\overline{du_{1,1}^{cell,roll}} - \overline{du_{2,2}^{cell,roll}})/\lvert d\epsilon_{22}\rvert$		−0.02	−0.12
K	Rigid-rotation, $\sum(\overline{du_{1,1}^{cell,rigid\text{-}rot}} - \overline{du_{2,2}^{cell,rigid\text{-}rot}})/\lvert d\epsilon_{22}\rvert$		0.33	1.93
L	Total distortion, $(d\epsilon_{11} - d\epsilon_{22})/\lvert d\epsilon_{22}\rvert$	$\sum =$	1.13	2.56

The results are for simulated biaxial compression of a 2D assembly of circular disks. The assembly deformation is a area-weighted tally of the micro-deformations within void cell regions.

- At small strains, both the normal and tangent motions produce material distortion, and they do so in roughly equal measure (Table 7, rows D and E). At large strains, the distortion is almost entirely attributed to inter-particle movements that are tangent to the contacts.
- At zero strain, volume change is almost entirely attributed to contact deformation, with almost no contribution from the other forms of relative particle translation (Table 8, rows A–C). This result suggests that a mean-strain approach to estimating the bulk modulus would be particularly successful at small strains. At large strains, volume change results primarily from the rigid-rotations of particle pairs (Table 8, row E). The dominant effect of tangent motions on the dilation at large strains was noted in the first observation. For circular disks, the tangent motions are expressed as combinations of contact sliding (i.e., tangent contact deformation, both elastic and slip), contact rolling, and rigid-rotation. Tables 7 and 8 suggest that contact sliding has a small compressive effect, but that this effect is counteracted by the dilatant effect of the rigid-rotations.
- At small strains, distortion mainly results from contact deformations (both normal and tangential), but also from the rigid-rotations of particle pairs (Table 8, rows G–I and K). At large strains, most distortion is attributed to the rigid-rotations, with a smaller contribution from contact sliding. This smaller contribution of contact sliding is predominantly attributed to frictional slip, rather than to the elastic contact deformations (either normal or tangential).
- As expected, frictional slip has very little influence on deformation at the start of loading. At large strains, slip has significant compressive and distortional effects.

Table 8 also shows that contact rolling contributes little to the overall deformation of the assembly. The small cumulative influence of rolling does not mean, however, that contact rolling is not active in material deformation. At the peak state, the local, individual void cell contributions of rolling, $du_{i,j}^{cell,roll}$, were large

and varied, but the local positive and negative contributions canceled each other in our tally of the cumulative effect.

6. Conclusion

The paper has focused on numerical experiments to analyze rotations and rolling in granular assemblies, and on their role in the overall material deformation. Different scales were analyzed: individual particle rotations, contact rolling between pairs of particles, material rotations of void cells, and rotational patterns on extended domains. The most important findings are as follows:

- Confirming the results of Jenkins and La Ragione (2003) and Calvetti et al. (1997), the average *particle rotation* can differ slightly from the mean continuum rotation of an assembly, although the average particle rotation is small in comparison to the rotational fluctuations of individual particles. The particle shape does not have an appreciable effect on the average of the particle rotations, but, especially prior to the peak stress state, the statistical scatter is larger in the case of circles and spheres than for ovals and ovoids. The most rapidly rotating particles are aligned in chain-like patterns. Particle rotations become more rapid with increasing strain until the peak stress is attained.
- The interaction between two contacting particles is a combination of contact deformation, *contact rolling*, and a *rigid-rotation* of the pair. Different measures of contact rolling were introduced. These measures are closely correlated with each other, so that each could serve as the basis of a kinematical state variable in future constitutive theory. Concerning the spatial distribution of contact rolling, we found that (a) the directions of the rolling vectors around an individual particle correlate strongly with each other; and (b) except at the initial strain, the most rapidly rolling contacts form strip-like domains that coincide with the most rapidly deforming regions of the assembly. Particle rotations have a softening effect, by reducing the contact deformation that would otherwise be produced by the particle translations.
- A micro-level state variable belonging to the individual grains, called the *rolling curl* was defined. Using this quantity, we analyzed spatial correlations between the rolling motions of particles, and the results give clear evidence of a gear-like pattern of rolling motions.
- *Material rotations* were calculated as the anti-symmetric part of the velocity gradient within material void cells, and the material rotations were compared with the particle rotations. At small strain, the material rotations were smaller and less scattered; but at the peak stress state, the material rotations were nearly as large as the particle rotations in both their averages and their dispersions.
- The *deformations of void cells* were partitioned in two different ways, and the significance of the deformation parts were appraised during the simulated deformation processes. Though contact rolling motions made a small contribution to the overall deformation of the assemblies, the rolling contributions in the individual voids were large.

In future experimental studies we would like to learn how the rolling and deformation behaviors are influenced by particle characteristics, such as contact friction, and by geometrical features, such as grain size distribution and particle shape. We also plan to analyze unloading and cyclic loading processes, to supplement the monotonic loadings that were exclusively considered in the present paper. We expect that the results of the current and future studies will provide a sound basis for developing a constitutive theory that incorporates the effects of rolling motions and particle rotations.

Acknowledgement

The work was funded in part by the grant OTKA 31889. This support is gratefully acknowledged.

References

Bagi, K., 1993. On the definition of stress and strain in granular assemblies through the relation between micro- and macro-level characteristics. In: Thornton, C. (Ed.), Powders & Grains 93. A.A. Balkema, Rotterdam, Netherlands, pp. 117–121.

Bagi, K., 1996a. Geometrical modeling of granular assemblies. Acta Technica Acad. Sci. Hung. 107 (1–2), 1–16.

Bagi, K., 1996b. Stress and strain in granular assemblies. Mech. Mater. 22 (3), 165–177.

Bagi, K., Kuhn, M.R., 2004. A definition of particle rolling in a granular assembly in terms of particle translations and rotations. J. Appl. Mech.

Bardet, J.P., 1994. Observations on the effects of particle rotations on the failure of idealized granular materials. Mech. Mater. 18 (2), 159–182.

Calvetti, F., Combe, G., Lanier, J., 1997. Experimental micromechanical analysis of a 2D granular material: relation between structure evolution and loading path. Mech. Cohesive-Frictional Mater. 2 (2), 121–163.

Chang, C.S., Misra, A., 1989. Computer simulation and modelling of mechanical properties of particulates. Comput. Geotech. 7 (4), 269–287.

Cundall, P.A., Strack, O.D.L., 1979. A discrete numerical model for granular assemblies. Géotechnique 29 (1), 47–65.

Cundall, P.A., Strack, O.D.L., 1983. Modeling of microscopic mechanisms in granular material. In: Jenkins, J., Satake, M. (Eds.), Mechanics of Granular Materials: New Models and Constitutive Relations. Elsevier Science, Amsterdam, The Netherlands, pp. 137–149.

Daudon, D., Lanier, J., Jean, M., 1997. A micromechanical comparison between experimental results and numerical simulation of a biaxial test on 2D material. In: Behringer, R.P., Jenkins, J.T. (Eds.), Powders & Grains 97. A.A. Balkema, Rotterdam, Netherlands, pp. 219–222.

Dedecker, F., Chaze, M., Dubujet, P., Cambou, B., 2000. Specific features of strain in granular materials. Mech. Cohesive-Frictional Mater. 5 (3), 173–179.

Iwashita, K., Oda, M., 1998. Rolling resistance at contacts in simulation of shear band development by DEM. J. Engrg. Mech. 124 (3), 285–292.

Jenkins, J.T., La Ragione, L., 2003. The role of particle spin in a granular material. In: Bagi, K. (Ed.), Quasi-Static Deformations of Particulate Materials, Proc. of the QuaDPM'03 Workshop, August 25–28, Budapest, Hungary.

Khidas, Y., Ammi, M., Delannay, R., Schliecker, G., 2001. Experimental study of friction and rotational modes in a cylinder packing under shear stress. In: Kishino, Y. (Ed.), Powders & Grains 2001. A.A. Balkema, Lisse, pp. 389–392.

Koenders, M.A., 1987. The incremental stiffness of an assembly of particles. Acta Mechanica 70, 31–49.

Kruyt, N.P., Rothenburg, L., 1996. Micromechanical definition of the strain tensor for granular materials. J. Appl. Mech. 118 (3), 706–711.

Kuhn, M.R., 1999. Structured deformation in granular materials. Mech. Mater. 31 (6), 407–429.

Kuhn, M.R., 2004. Are granular materials simple? An experimental study of strain gradient effects and localization. Mechanics of Materials, in press.

Kuhn, M.R., 2003a. Heterogeneity and patterning in the quasi-static behavior of granular materials. Granular Matter 4 (4), 155–166.

Kuhn, M.R., 2003b. Smooth convex three-dimensional particle for the discrete element method. J. Engrg. Mech. 129 (5), 539–547.

Kuhn, M.R., 2004a. Boundary integral for gradient averaging in two dimensions: application to polygonal regions in granular materials. Int. J. Numer. Methods Engrg. 59 (4), 559–576.

Kuhn, M.R., 2004b. Rates of stress in dense unbonded frictional materials during slow loading. In: Antony, S.J., Hoyle, W., Ding, Y. (Eds.), Advances in Granular Materials: Fundamentals and Applications. Royal Society of Chemistry, London, UK.

Kuhn, M.R., Bagi, K., 2004. An alternative definition of particle rolling in a granular assembly. J. Engrg. Mech. 130 (7), 826–835.

Kuhn, M.R., Bagi, K., submitted for publication. On the relative motions of two rigid bodies at a compliant contact: application to granular media.

Lanier, J., 2001. Micro-mechanisms of deformation in granular materials: experiments and numerical results. In: Vermeer, P.A., Diebels, S., Ehlers, W., Herrmann, H.J., Luding, S., Ramm, E. (Eds.), Continuous and Discontinuous Modelling of Cohesive-Frictional Materials. Springer, Berlin, pp. 163–171.

Lanier, J., Jean, M., 2000. Experiments and numerical simulations with 2D disks assembly. Powder Technology 109 (1), 206–221.

Lin, X., Ng, T.T., 1997. A three-dimensional discrete element model using arrays of ellipsoids. Géotechnique 47 (2), 319–329.

Marcher, T., Vermeer, P.A., 2001. Macromodelling of softening in non-cohesive soils. In: Vermeer, P.A., Diebels, S., Ehlers, W., Herrmann, H.J., Luding, S., Ramm, E. (Eds.), Continuous and Discontinuous Modelling of Cohesive-Frictional Materials. Springer, Berlin, pp. 89–110.

Matsushima, T., Saomoto, H., Tsubokawa, Y., Yamada, Y., 2003. Observation of grain rotation inside granular assembly during shear deformation. Soils Found. 43 (4), 95–106.

Misra, A., Jiang, H., 1997. Measured kinematic fields in the biaxial shear of granular materials. Comput. Geotech. 20 (3), 267–285.

Molenkamp, F., 1984. Decomposition of velocity gradient into interparticle slip and rolling. Soils Found. 24 (1), 17–33.

Montana, D.J., 1988. The kinematics of contact and grasp. Int. J. Robotics Res. 7 (3), 17–32.

Oda, M., Iwashita, K., Kakiuchi, T., 1997. Importance of particle rotation in the mechanics of granular materials. In: Behringer, R.P., Jenkins, J.T. (Eds.), Powders & Grains 97. A. A. Balkema, Rotterdam, Netherlands, pp. 207–210.

Oda, M., Konishi, J., Nemat-Nasser, S., 1982. Experimental micromechanical evaluation of strength of granular materials: effects of particle rolling. Mech. Mater. 1 (4), 269–283.

Potapov, A.V., Campbell, C.S., 1998. A fast model for the simulation of non-round particles. Granular Matter 1 (1), 9–14.

Roux, J.N., Combe, G., 2003. On the meaning and microscopic origins of quasistatic deformation of granular materials. In: Proc. 16th ASCE Engineering Mechanics Conference, vol. 759. ASCE, pp. 1–5.

Satake, M., 1993. New formulation of graph-theoretical approach in the mechanics of granular materials. Mech. Mater. 16, 65–72.

Tamura, T., Koike, W., Sakurai, Y., 1998. Mechanics of assembly of rigid particles. In: Adachi, T., Oka, F., Yashima, A. (Eds.), Localization and Bifurcation Theory for Soils and Rocks. A.A. Balkema, Rotterdam, Netherlands, pp. 181–188.

Thornton, C., Antony, S.J., 2000. Quasi-static shear deformation of a soft particle system. Powder Tech. 109 (1), 179–191.